ABSTRACT

Title of thesis: DOSE AND IMAGE QUALITY CONSIDERATIONS IN COMPUTED TOMOGRAPHY

Samir F Abboud, Master of Science, 2011

Thesis directed by: Professor Iacovos Kyprianou
Department of Bioengineering

The increased use of Computed Tomography as an imaging modality is of concern because of the growing body of evidence linking radiation exposure to cancer incidence. However, a framework does not yet exist for balancing the immediate needs of the clinical task (image quality) with future risks due to the imaging procedure (dose).

We developed a method to estimate the shape and thickness of materials yielding attenuation equivalent to that of bow-tie-shaped filters in clinical scanners. The results are especially useful for accurate modeling in Monte Carlo simulations of radiation transport.

We then investigated measures of dose and image quality using both simulation and laboratory experimentation. We found that current measures of dose are robust under current clinical conditions. We also found that measures of image quality are object and task specific.

Dose and Image Quality Considerations in Computed Tomography

by

Samir F Abboud

Thesis sumbitted to the Faculty of the Graduate School of the
University of Maryland, College Park in partial fulfillment
of the requirements for the degree of
Master of Science
2011

Advisory Committee:
Professor Iacovos Kyprianou, Chair/Advisor
Professor Yu Chen
Professor Yang Tao

Acknowledgments

I owe many thanks to all the people who have made this work possible.

First and foremost I'd like to thank my advisor, Professor Iacovos Kyprianou for giving me the opportunity to work in an unrivaled environment for the past two years. He has always been available to answer my many questions, and provide direction in new avenues that I had not previously considered, or even knew existed. Working and learning with him was the cornerstone of my graduate education. Without his expertise, this work would not have been possible.

Thanks are due to Professor Yu Chen and Professor Yang Tao for agreeing to serve on my thesis committee and for sparing their invaluable time reviewing the manuscript.

My colleagues at the FDA CDRH DIAM Imaging Physics laboratory have eased my graduate life in many ways and deserve a special mention. Andreu Badal helped me start-off understanding and working with the Monte Carlo simulation code in a user-friendly format. Claudia Brunner provided help by teaching me how to operate the bench-top, cone-beam CT system. My lab group-mates Haimo Liu and Songxiang Gu have been very helpful in thinking laterally about my projects and in the nitty-gritty details of the various codes and programs we used. I'd also like to thank Dorothea Brosius for providing the LaTex style files and templates for writing this thesis.

I would be remiss if I didn't acknowledge help and support from some members of the larger FDA family. Stanley Stern's help with technical details of CT systems

and dosimetry used in Chapters 2 and 4 is highly appreciated, as is the support from Robert Jennings, without whom the project in Chapter 4 would never have occurred. Kyle Myer's willingness to take time to explain the mathematics of imaging science is deeply appreciated. Additionally, I must thank Eugene O'Bryan, Jonathan Boswell, Mary Walker and the radiation metrology lab.

Thank you Mahadevappa Mahesh for working with us to collect the clinical scanner data used in Chapter 4.

It goes without saying that these projects would not have been possible without the work of Bruce Fleharty and Randy Bidinger, who fabricated the phantoms and custom parts I used in the experiments.

I would like to acknowledge financial support from the FDA Office of Women's Health through an appointment to the Research Participation Program at the FDA Center for Devices and Radiological Health administered through the Oak Ridge Institute for Science and Education according to an interagency agreement between the U.S. Department of Energy and the U.S. Food and Drug Administration.

There are always more to thank than I can recall, and I apologize to those whom I have inadvertently forgotten to mention here.

Last, but not least, I must thank my family. My mother and my father for teaching me the value of education, and supporting me as I took the long road. My brothers and sisters for keeping things fun, and keeping me sane.

Table of Contents

Chapter 1

Overview

1.1 Introduction

Computed Tomography (CT) generally refers to the process by which three dimensional volumes are reconstructed using multiple X-ray projection images from different angles. CT has been clinically available since the early 1970's, and has seen use as a diagnostic tool for clinical scenarios ranging from cancer diagnosis to acute trauma. The most common modern CT systems consist of an X-ray tube and detector array pair mounted in a gantry. The tube and detector array rotate about the volume of interest (often a patient) as it is translated through the field of view and projection images are collected. These projection images are then used in the three-dimensional reconstruction of the volume of interest. The main advantages of CT versus traditional projection X-ray imaging is that it allows for the the removal of overlying anatomy from the plane of interest and offers increased contrast between structures.

Since the introduction of the first CT scanner (The EMI Mark 1), technological improvements have been made reducing scan and reconstruction times. However, increases in volume of coverage tend to increase dose per procedure.[3] Additionally, the ease and speed with which CT scans can now be obtained has resulted in an increasing number of procedures performed annually.[16] The collective radiation

dose from all medical imaging procedures increased over seven-fold from 1990 to 2006, and while CT scans account for only 18 percent of procedures performed, they contribute over 50 percent of this collective dose.[4] The advancement of further applications of CT (e.g. cardiac CT angiography, colonoscopy, and interventional CT) is also expected to fuel the growth of CT use. This is a concern because exposure to ionizing radiation has been linked by a growing body of evidence to the incidence of solid cancer and leukemia.[3]

Determining the "right" amount of radiation for a CT scan is a non-trivial proposition. The difficulty lies in minimizing the radiation necessary to achieve adequate image quality. Or, put another way, using the lowest possible dose to create an image suitable for the clinical task. Before attempting to answer this question, however, one must first address what metrics are to be used in measuring dose and image quality.

There is question as to whether the current CT dosimetry and image-quality metrics are suitable for modern CT technology. The current dosimetry system is based on a metric developed at the FDA in the 1980's.[56] However, for modern scanners with larger fields-of-view, these metrics may lose accuracy and applicability. Image quality is often reported in terms of its sharpness, usually characterized and reported as a spread function, often with additional calculation of a modulation transfer function.[52, 31, 32] This linear systems approach assumes that all objects being imaged are transferred in the same way, which is not true for CT systems (and even less so when non-linear reconstruction algorithms are used). The reasons for this will be explored further later in the thesis. Furthermore, there is no meaninful

metric linking CT image quality with radiation dose that has found widespread acceptance in the medical physics community.

This thesis provides a tool for modeling clinical X-ray sources without knowledge of proprietary information. The implementation of these source models into existing Monte Carlo codes will allow for simulation of scanner specific imaging procedures. Combined with existing anthropomorphic phantoms, these simulations will provide insight into organ dose distribution in "average" patients. Furthermore, they will allow for the testing of new protocols or devices *in silico*. This thesis also describes current dosimetry metrics and image quality metrics. It will be shown that scanners with large fields-of-view require small modifications of current dosimetry metrics. However, the usefulness of these metrics remains potent. It will also be shown that linear systems theory based metrics of image quality are task specific. This is not to mean that they do not apply to CT, but rather that consideration must be taken when implementing the estimation of such metrics.

1.2 Basic Principles of CT

Although the true mathematical details of CT reconstruction are beyond the scope of this work, a basic review is necessary to understanding the experiments and results presented in later chapters. The fundamental mathematics of CT reconstruction were established over five decades prior to construction of the first clinical scanner. J. Radon, in 1917, proved that with a complete, infinite set of projections of a two- or three-dimensional object, the original could be reproduced.[50] Though

Radon was working with gravitational theory, his proof had an important application in medical imaging; the internal structure of an object could be reconstructed using multiple projections of that object from different angles.

In its most elementary form, CT reconstruction is an exercise in linear algebra.[35, 21, 36, 19] If an x-ray beam is incident on one side of the object with intensity I_0, and a measurement is taken of the transmitted x-ray intensity, I_t, then the relationship between the two is given by:

$$I_t = I_0 e^{-\mu t}, \tag{1.1}$$

where t is the thickness of the attenuating region and μ is the average linear attenuation coefficient along the path between the source and the detector. Rearranging and taking a natural logarithm yields:

$$ln(\frac{I_0}{I_t}) = \mu t, \tag{1.2}$$

revealing the true parameter of interest, μ.

A more complex case would be non-uniform object that we have divided into a uniform array of four elements (see Figure 1.1). Taking two projections of this object yields four transmission measurements, yielding a fully constrained system of four equations with four unknown average linear attenuation coefficients (corresponding to the average attenuation of each element). This system of equations can be solved readily, yielding the average attenuation of each of the four elements. [1]

[1]It is important to note that these examples assume a monochromatic beam. Because attenuation coefficients actually vary with the energy of the incident photon, correction factors must be incorporated in clinical CT systems. These factors account for the heterochromatic nature of x-rays used in commercial scanners. A geometric correction factor is also necessary to reconcile the differences between the Cartesian picture array (squares) and the radial nature of the source rotation about the object.

Figure 1.2 shows what two projections of a more complicated theoretical object of interest might look like. In order to reconstruct this object faithfully, a higher density of array elements is needed than the four-element example. As the number of elements within the array grows, the number of projections required to fully constrain the system grows as well. Solving this system directly becomes computationally expensive.

Fortunately, some basic strategies for dealing with this problem have been devised including back-projection (with and without filtering), iterative reconstruction, and Fourier analysis. The most common method in use today is the filtered back-projection method.[19] The volume of interest in this method is reconstructed by algorithmically reversing the steps used during acquisition. Each attenuation value measured is smeared along the path from the source to the detector equally. As this smearing is performed for many projections, an image of the volume is built up. The filtering portion of filtered back-projection is necessary to re-weight the data because of geometric issues arising from the conversion between polar coordinates and rectangular coordinates.[35] Iterative reconstruction assumes values for the matrix of attenuation coefficients, and then compares the assumed values to measured projection values. Corrections are made according to an algorithm, and the process is repeated until a tolerance threshold is reached.

In general, these basic approaches are referred to as linear reconstructions because only linear mathematical operations are used (i.e. the same operation is performed on the whole of the image, and it is easily invertable). More modern scanners may also include non-linear reconstruction algorithms. These include tech-

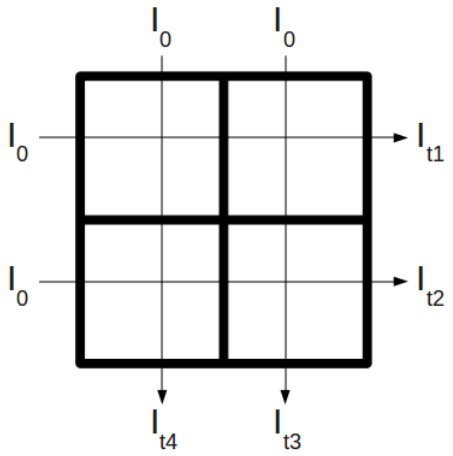

Figure 1.1: Two projections fully constrain a four-element system.

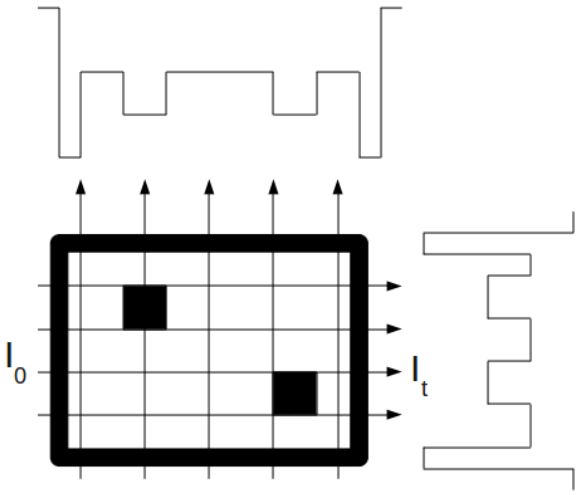

Figure 1.2: Two projection images of a theoretical object.

niques for selectively sharpening parts of the image to improve edge detection while smoothing other parts to reduce noise. These algorithms have also been used to suppress artifacts. While these approaches qualitatively improve image quality, it is unknown how they affect quantitative measures of image quality, and ultimate clinical performance.

1.3 Concepts of Dosimetry

The radiation dose to the patient from CT procedures is an important issue. It is of interest because radiation quantities provide an idea of the risk of biologic damage associated with exposure to that radiation. The interaction of radiation with biology produces a range of effects that include skin reddening, hair loss, acute cataract, temporary or permanent fertility loss, hematopoietic syndromes, and radiation induced carcinogenesis.[19]

Before discussing methods of measuring radiation dose, it is important to distinguish the term exposure from dose. Exposure relates to the number of ionizations in air that are produced by x-ray photons. Dose refers to the amount of radiation deposited in a body of interest, usually the patient.

In current clinical practice, the primary radiation dose metric is the Computed Tomography Dose Index (CTDI). The CTDI is a measurement of the dose delivered to a polymethyl methacrylate (PMMA) right-round cylindrical phantom for the imaging procedure performed. Derivatives of the CTDI are used to express average doses delivered in a volume of interest of the cylinder, or total dose to the cylinder,

or effective dose, which attempts to assess the potential biologic risk due to a CT procedure.[1]

However, the CTDI was defined in the early 1980's.[56] There is concern that as modern scanners evolve to have ever larger fields-of-view, the associated increased beam-width along the z-axis tends to grow to a size that no longer can be evaluated in the CTDI paradigm. Therefore, exploring the behavior of dose profiles in the CTDI PMMA phantoms is necessary to determine if the metrics are still stable under modern scanning conditions.

1.4 Image Quality Metrics

The fundamental image properties are contrast and spatial resolution.[19] Contrast refers to the difference in the gray scale of the image, which in CT are produced by differences in tissue composition (corresponding to different attenuation coefficients). Resolution is the ability to see small details, and for photon based imaging modalities is theoretically limited by the wavelength of the photon used to probe the object's details. In practice, however, the spatial resolution of clinical imaging systems is lower than this theoretical limit. In comparison to projection imaging, the contrast of CT is much better. This is because the tomographic reconstruction removes overlying structures. However, CT generally has worse spatial resolution.

A useful metric of spatial resolution is the Point Spread Function (PSF). In the spatial domain, the PSF is defined as the response of the imaging system to a single point input. Knowledge of the complete PSF is useful because it allows

for a prediction of the image output given the object input. It is beneficial to also study resolution in the frequency domain. Frequency domain measurements are reported in terms of line pairs per millimeter, and are thought of as sine wave inputs into the imaging system and blurred by the PSF. The effect of the blurring is to reduce the contrast between the crests and troughs of the sine wave, and if the frequency is high enough, the waves are blurred together and indistinguishable in the image produced. This blurring effect is dependent on the frequency of the sine wave input, and the frequency dependence of the blurring is called the Modulation Transfer Function (MTF). The MTF of an imaging system is the currently accepted method of reporting the resolution properties of an imaging system. However, the calculation of the MTF for a real imaging system makes some limiting assumptions. It assumes that the system be stationary (that the PSF does not change as a function of position in the image) and shift-invariant (that the noise in the system does not change with position in the image). It also assumes that the system is linear, i.e. all objects are transferred from the object plane to the imaging plane in the same way. It is possible that these assumptions are broken in real CT imaging systems, and therefore it is important to investigate what systemic errors are introduced into image quality measurements by these effects.

1.5 Outline of the Thesis

The work presented here is divided into three steps. First, a tool for incorporating CT-scanner specific source models into Monte Carlo simulations is reported.

Next, radiation dosimetry concepts and metrics are discussed. Finally, image quality evaluation is described.

Monte Carlo techniques allow for the simulation and testing of CT systems without collecting large amounts of data physically. However, manufacturers place differing amounts of filtration in the beam path and often keep this information proprietary (as a trade secret). In order to perform realistic simulations, however, the Monte Carlo code must have x-ray spectra that match the filtered spectra from these clinical systems as closely as possible. To enable simulations using scanner-specific spectra without disclosing proprietary information from manufacturers, Chapter 2 demonstrates the implementation of a technique for calculating equivalent spectra from a few simple measurements. Using common equipment (aluminum filters and an ionization chamber), we demonstrate that it is possible to estimate accurately matched equivalent filters to the unknown filters in the CT system. With this tool, researchers can simulated specific scanners without being dependent on disclosure from manufacturers, and without risking exposure of proprietary information.

Chapter 3 discusses radiation dosimetry. First, the framework of the Computed Tomography Dose Index (CTDI) metric and its derivatives are described. Then, the behaviors of both longitudinal and radial dose profiles in CTDI phantoms are reported. It is shown that CTDI metrics are applicable to current CT imaging systems, and with a small adjustments can be applied to proposed future systems.

In Chapter 4, the modulation transfer function (MTF) is investigated. This is accomplished by testing of multiple methods of estimating an imaging system's image quality in terms of the MTF. A comparison of methods is made with an eye

towards clinical applicability.

Chapter 5 is a summary of conclusions. It also includes final remarks and suggestions for further avenues of investigation.

Chapter 2

Angle dependent spectra of clinical CT systems

2.1 Introduction

Exposure to ionizing radiation has been linked by a growing body of evidence to the incidence of solid cancer and leukemia.[3] Additionally, exposure exceeding deterministic thresholds can yield erythema, hair epilation and acute cataract. The collective radiation dose from all medical imaging procedures increased over seven-fold from 1990 to 2006, and while CT scans account for only 18 percent of procedures performed, they contribute over 50 percent of this collective dose.[4] Because increasing dose is of concern individually and collectively, efforts are being made to quantify radiation dose delivered to individual patients, including dose delivered to each organ, as well as average collective doses.[29, 58]

One approach that is favored is the use of Monte Carlo techniques to estimate radiation dose.[60] Knowledge of the complex spectra character of CT emissions is essential for Monte Carlo simulations of radiation transport and in the estimation of organ doses.[57] All commercial CT scanners make use of filtration to harden the x-ray beam. The proprietary aspect of the designs of shaped filters limits researcher's access to them and hence impedes accurate modeling of these spectra.

Turner *et al* described a method for estimating clinical CT-scanner spectra using half value layer (HVL) measurements and the bow-tie profile (exposure across the

fan beam) to determine an equivalent filter.[59] In this method, a "soft" tungsten-target spectrum is simulated to be transmitted through a hardening material such as aluminum. The composition and thickness of the material is varied until the HVL of the candidate spectrum is matched as closely as possible to experimental measurement along the central ray. The angle-dependent filtration path length of additional aluminum is then determined using the ratio of measured exposure at a given angle to the exposure along the central ray. While this method can estimate the relative number of photons in the off-centerline spectra, because only one material thickness is varied it cannot match both relative photon number and spectral shape. Another method is discussed theoretically by Boone,[15] in which a radiation monitor is placed at the periphery of the CT field, and kerma rate versus time is used to extract angle-dependent bow-tie filter attenuation. By taking these measurements at multiple kVp settings, an equivalent bow-tie filter can be estimated. However, to date this work has not been demonstrated in the clinical setting, and is limited by the need for a radiation monitor with high temporal resolution.

To properly frame the task addressed in the present work, it is important to recognize that filter materials can be compared on two bases – "quantitative" equivalence and "qualitative" equivalence. For two filters to be quantitatively equivalent, they must decrease the measured air kerma by the same amount for a specified incident x-ray spectrum. Quantitative equivalence, however, does not guarantee that the transmitted spectra will have the same shapes. Two filters are qualitatively equivalent if they result in transmitted spectra that have the same relative spectral intensity distribution for a given incident spectrum, though not necessarily the same

absolute intensity. It is the task here to generate qualitatively equivalent spectra for use in Monte Carlo simulation.

In this section, we leverage published x-ray spectra, energy-dependent linear attenuation coefficients and kerma conversion factors[24] to provide a simple method of generating an equivalent bow-tie-shaping filter. First, we review the theory involved in matching spectral measurements to generated spectra. We then investigate with a simulated experiment the ideal accuracy limits of such an approach. Third, we validate the approach by laboratory measurements on known filters. We then generate an equivalent bow-tie-shaping filter evaluated from a clinical system and the associated angle dependent spectra for use with Monte Carlo simulation.

2.2 Methods

2.2.1 Theory

To find a filter that is qualitatively equivalent to an unknown filter, we begin with an empirical finding: the attenuation coefficients of any material whose K-edge does not encroach on the energy range of interest can be written as a linear combination of those of two other materials, provided they are sufficiently linearly independent.[46, 7] That is, an appropriate combination of two materials can be used to substitute for other materials in an x-ray path, and both resulting spectra would have good agreement in shape and intensity.

We assume *a priori* knowledge of a spectrum as it exits the anode (i.e., without any filtration whatsoever) from those of Report 78 of the Institute of Physics and

Engineering in Medicine.[24] We denote the mAs-normalized x-ray photon fluence of this unattenuated spectrum as Φ (number of photons/mm^2 mAs). The air kerma (K_a) produced by this spectrum is given by the expression:

$$K_a = \int k(E)\Phi(E)dE, \tag{2.1}$$

where $k(E)$ is the energy-dependent conversion factor that can be obtained from the literature. If there is an unknown attenuator between the x-ray tube and measurement device, the expression is modified by the attenuator:

$$K_a = \int k(E)e^{-\mu_{unk}(E)\times T}\Phi(E)dE, \tag{2.2}$$

where T is the equivalent thickness of the unknown attenuator. We can characterize the unknown attenuator in terms of a combination of two materials. For basis functions, we use the attenuation spectra of aluminum and polymethyl methacrylate (PMMA), two materials commonly used in the fabrication of clinical CT filters:

$$K_a = \int k(E)e^{-\mu_{Al}(E)\times T_{Al}}e^{-\mu_{PMMA}(E)\times T_{PMMA}}\Phi(E)dE. \tag{2.3}$$

Determining the two unknown thicknesses is an exercise in linear algebra.

2.2.2 Algorithm implementation

2.2.2.1 If mAs is known

In order to solve for T_{Al} and T_{PMMA}, at least two measurements of air kerma at the scanner isocenter must be taken, one free in air and one with added Al filtration. We evaluate expected air kerma per mAs versus notional thicknesses of PMMA and

Al for both the free-in-air and added-filtration cases. After taking experimental measurements of air kerma under the same respective conditions, using numerical methods we select T_{Al} and T_{PMMA} such that expected values of K_a per mAs match their corresponding measured values.

Figure 2.1 shows the contours of exposure in μGy/mAs associated with notional thicknesses of Al and PMMA for a 120 kVp beam. Figure 2.2 shows the contours of ratio of K_a after adding 10 mm of Al to K_a free-in-air. To solve for an equivalent filter using this approach, the two experimental measurements define contours on the two surfaces, and the intersection of the contours yields the thicknesses of PMMA and aluminum, the combination of which corresponds to an equivalent of the unknown filter.

2.2.2.2 If mAs is unknown

Typically, clinical CT scanners use a slot-scanning technique to acquire a projection image. Even though total mAs for the projection image is reported, this is not necessarily the same as the mAs that corresponds to the portion of the beam incident on the ionization chamber. A model for a bow-tie-shaped filter for Monte Carlo simulations can be developed by matching the spectral shape at each angle and the relative number of photons between the centerline and a given off-center angle. From Figure 2.2 we see that given the ratio of K_a with and without added filtration (determined for a particular angle), a range of different T_{Al} and T_{PMMA} can generate the same spectral shape. The relative number of photons at each an-

gle can then be determined by choosing T_{Al} and T_{PMMA} from one of the possible values (as determined from the contours of Figure 2.2) at the centerline. From the K_a per mAs (shown in Figure 2.1) that corresponds to the chosen T_{Al} and T_{PMMA}, we determine a reference mAs which is then used to obtain the relative number of photons at each off-center angle.

2.2.3 Simulated test case

A computer algorithm for solving equation (3) was implemented matching exposure and percent decrease of air kerma following known added filtration. To test the accuracy of this algorithm under ideal conditions, a test filter was modeled computationally from 2 mm beryllium, 2 mm glass, 0.05 mm copper and 3 mm PMMA to simulate some attenuating materials that could be used as filters in clinical systems. This test filter was used to attenuate 80, 100 and 120 kVp tungsten anode spectra. The calculated exposure and exposure decrement following additional filtration were used to generate an equivalent filter of aluminum and PMMA. The spectra that resulted following attenuation with the test filter were compared to the spectra following attenuation with the equivalent filter estimated by our method, and percent agreement is reported. Further, the equivalent filter thicknesses were compared to one another to investigate the influence of kVp on the calculated filtration.

2.2.4 Laboratory verification

In the laboratory, the algorithm was tested for its ability to recreate known filters of PMMA and aluminum. The x-ray tube used is a Varian B180 (Varian Corp., Salt Lake City, UT) with an inherent filtration of 1 mm Al. Air kerma measurements were performed with a Radcal model 9010 radiation monitor with a 0.6 cm^3 ionization chamber (Radcal Corp., Monrovia, CA), the smallest chamber available to us. Four thickness combinations were used, summarized in Table 2.1. The source-to-detector distance was 75 cm.

The process was repeated a second time without knowledge of mAs. The measured filter material thicknesses were the same as those listed in Table 2.1. To illustrate that the shape of the spectrum is constant on a contour line in Figure 2.2, we selected three pairs of material thicknesses that would result in the measured ratio of K_a with and without added filtration for the first thickness combination (2 mm al, 10 mm PMMA). The resulting filtered spectra were all normalized by area and compared with the expected spectrum resulting from the known filter composition. We then calculated a "reference" mAs for each of the three estimated thickness pairs. This was done by dividing the measured free-in-air kerma (in mGy) by the free-in-air kerma (in mGy/mAs) taken from Figure 2.1. This reference mAs was used to normalize the other free-in-air kerma measurements in the experiment to units of mGy/mAs. This is done to fix the relative number of photons among the filters. That is, using Figure 2.2 fixes the shape of each characterized spectrum, and using the reference mAs and Figure 2.1 fixes the relative number of photons.

2.2.5 Application to a clinical CT system

To study the practicability of implementation and plausibility of results associated with a CT system used clinically, the algorithm was applied to characterize the filtration associated with a Toshiba Aquilion 64 at Johns Hopkins University Hospital. With the source in scan-projection mode and positioned horizontally to reduce scatter from the patient couch, air kerma measurements at 120 kVp tube voltage were taken at five points from the central ray toward the peripheral ray of the fan beam, starting at the scanner isocenter and then going up +30, +60, +80 and +110 mm covering the full field of view. Air kerma measurements were performed with a Radcal model 9010 radiation monitor and a 0.6 cm^3 ionization chamber. The ionization chamber was supported by a long thin stand as far away as possible from the patient couch to reduce scatter effects. Scan conditions of operation were those for a CT perfusion scan (without movement of the patient couch) with a small field of view, and so the small bowtie filter was in place. Air kerma was measured with zero or 16-mm filtration of 99.5% pure aluminum at each point. The experimental setup is shown in Figure 4.5. These measurements were used to calculate angle dependent equivalent thicknesses of aluminum and PMMA, and interpolation was used to create angle-dependent profiles of the aluminum and PMMA thicknesses comprising an equivalent of the shaped filtration.

2.3 Results

2.3.1 Simulated test case

The spectra computed from the test filter described in section 2.3 and from the equivalent filter are shown in figures 2.4(a), 2.4(b) and 2.4(c). The distributions show excellent matching qualitatively, so the percent agreement versus photon energy is shown in figures 2.5(a), 2.5(b) and 2.5(c). The percent difference was not calculated for energies lower than 20 kV because photon counts are low in this region. The calculated thicknesses for equivalent aluminum and PMMA filters varied by less than 5 percent.

2.3.2 Laboratory filtration matching

Calculated versus measured thicknesses of aluminum and PMMA are summarized in Table 2.1. At most, the calculated thicknesses of aluminum deviate by less than 6% from measured values, whereas the deviation of PMMA is larger, ranging between 0.5 and 8.5%. For the result with the largest deviation, which was 3 mm aluminum and 20 mm PMMA, the percent agreement between the spectra is shown Figure 2.6.

With mAs unknown, we selected three points in Figure 2.2 that matched the measured ratio of K_a for the first material thickness combination (2 mm al and 10 mm PMMA). T_{Al} was set to 0.5, 1, or 2 mm, and the corresponding T_{PMMA} was found for each T_{Al}. The resulting estimated spectra, normalized by area, are shown in Figure 2.7(a). The reference mAs was calculated for each of the three estimated

thickness combinations, and was used to normalize the free-in-air kerma measurements for the other measured material thickness combinations. Then their filtered spectra were characterized, and are plotted in Figures 2.7(b), 2.7(c), and 2.7(d). Though three spectra are plotted in each figure, they are almost indistinguishable. To facilitate comparison, percent agreement with respect to energy is shown for each material thickness combination in Figures 2.8(a), 2.8(b), 2.8(c), and 2.8(d). In regions where photon counts were highest, percent agreement stayed within five percent of the expected spectrum as calculated using the known thicknesses of filtering materials, and even in regions with lower photon counts, percent agreement stayed within 8 percent of the expected spectrum.

2.3.3 Representation of the bow-tie-shaped filter for a clinical CT scanner

The measurements at the five points from a Toshiba Aquilion 64 were used to calculate equivalent thicknesses of PMMA and aluminum, and a profile of the filter was interpolated from these points. This profile is shown in figure 2.9.

2.4 Discussion

A method for determining angle-dependent equivalent filtration and spectra of a CT scanner was developed and tested computationally, experimentally and with a clinical CT scanner. For shaped filters used in CT, the method matches not only decrement in intensity with changing angle, but also spectral shape, which cannot

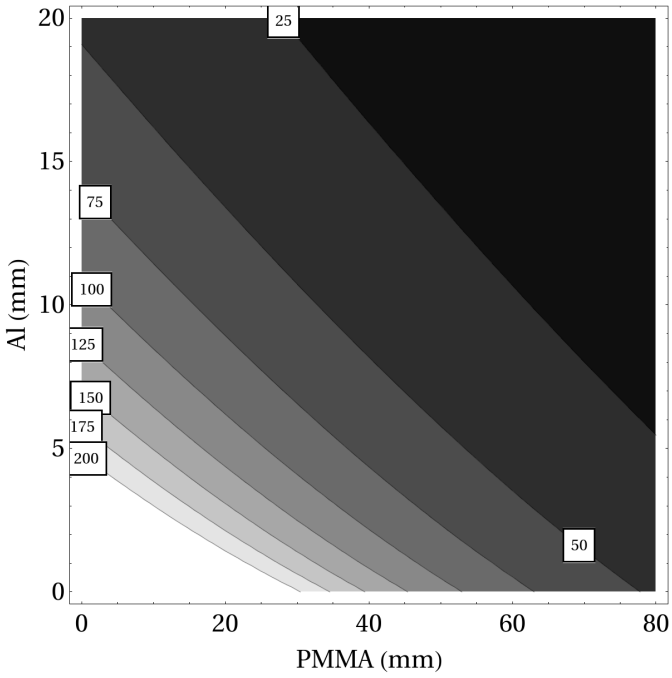

Figure 2.1: The air kerma (nomalized as μGy/mAs) expected[24] at 75 mm following attenuation of a 120-kVp x-ray beam by varying notional thicknesses Al and PMMA representing the inherent plus bow-tie filtration. The boxes label curves with constant values of mAs-normalized air kerma.

Filter Material Thickness (mm)			
Measured		Calculated	
Al	PMMA	Al	PMMA
2	10	2.01	10.05
3	10	2.99	10.85
6	10	5.78	10.48
3	20	3.16	18.75

Table 2.1: Measured thicknesses and calculated thicknesses of aluminum and PMMA.

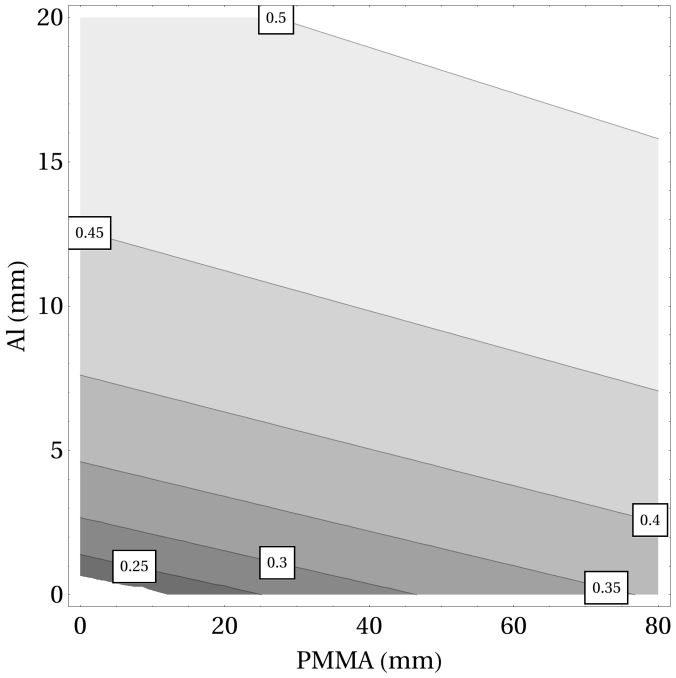

Figure 2.2: Contours of the ratio of K_a after adding 10 mm of Al to K_a free-in-air for a 120-kVp x-ray beam for different notional thicknesses of aluminum and PMMA representing inherent plus bow-tie filtration. The boxes label curves with constant ratios.

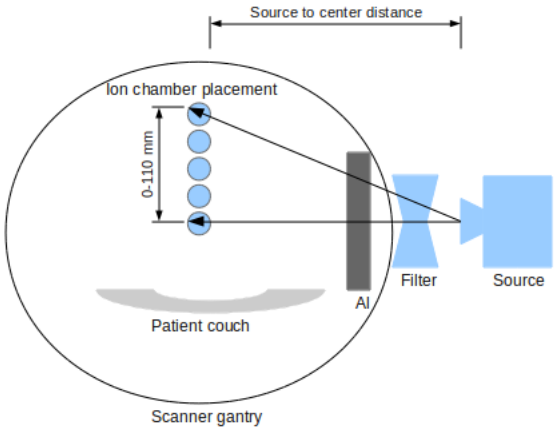

Figure 2.3: Schematic of measurements taken from a Toshiba Aquilion 64. The scanner is in scan-projection mode to reduce scatter and attenuation from the patient couch.

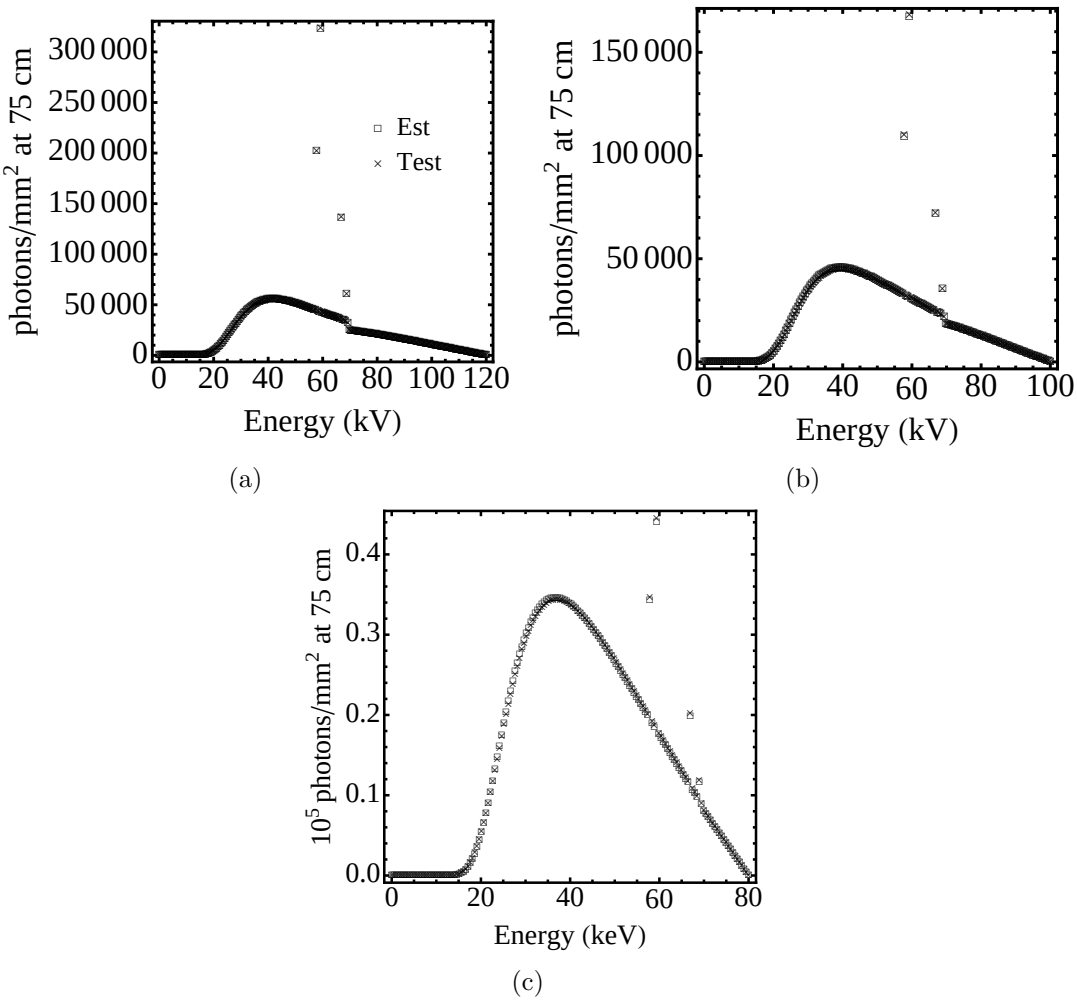

Figure 2.4: Spectra computed from a simulated test filter (crosses) and the estimated (Est) equivalent filter (squares) for (a) 120 kVp, (b) 100 kVp and (c) 80 kVp sources. The simulated test filter is described in section 2.3.

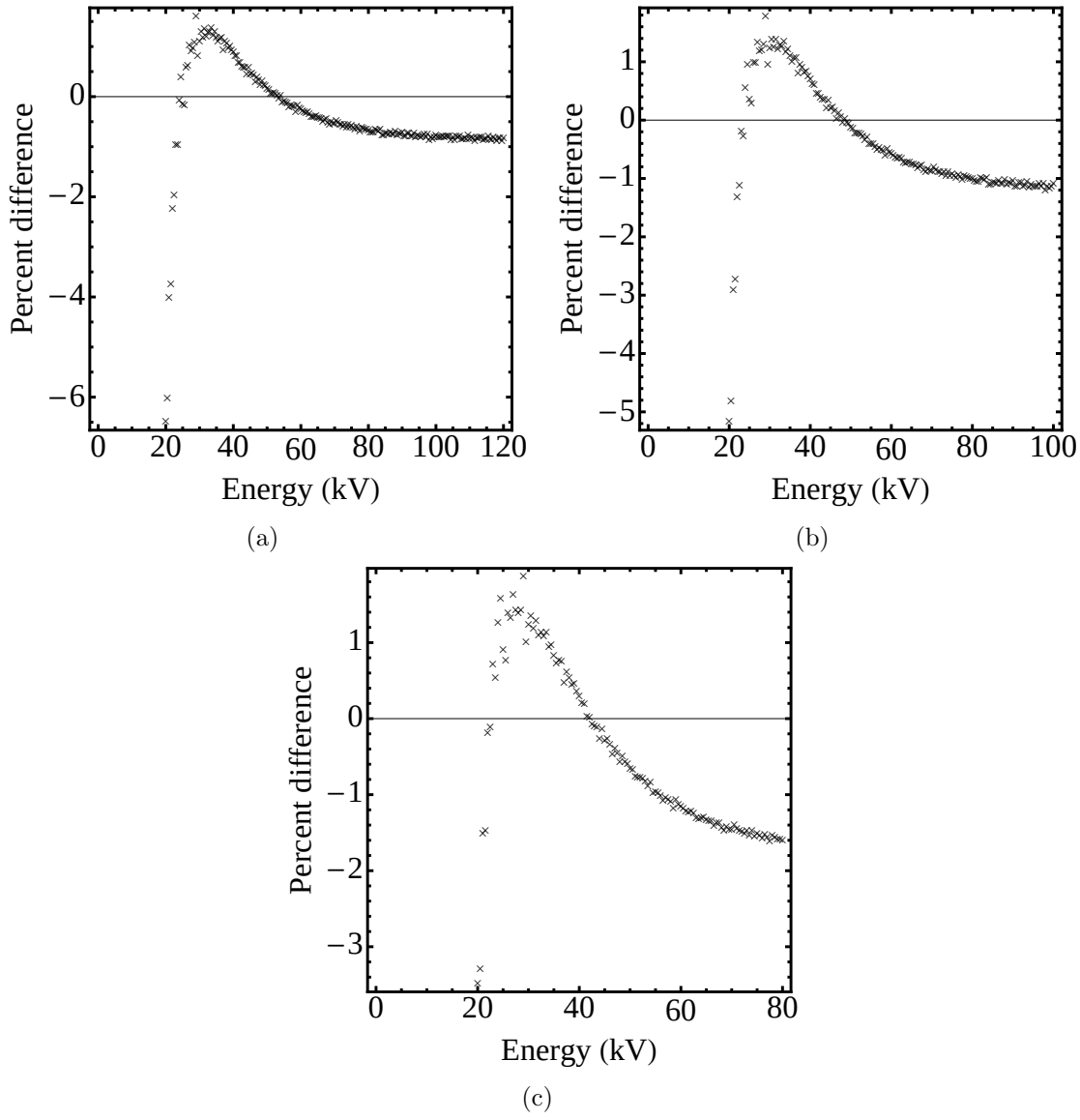

Figure 2.5: Percent difference between a simulated test filter and the estimated equivalent filter for (a) 120 kVp, (b) 100 kVp and (c) 80 kVp sources. The simulated test filter is described in section 2.3.

be accomplished by varying one thickness alone.

This method is intended for designing accurate Monte Carlo models of clinical CT scanners. Monte Carlo simulations can be used to estimate organ-specific and peak doses from particular medical imaging studies. The method is quick and easy to implement, as only two measurements per angle are needed. While knowledge of mAs reduced inaccuracy in the calculated spectrum, the algorithm using unknown mAs was demonstrated to be robust in that the calculated, normalized angle-dependent spectra (section 2.3.2) are not sensitive to assumed starting thicknesses.

For off-central-ray thickness calculations, the source-to-isocenter distance must be known. When making air kerma measurements with added filtration, care must be taken to select a thickness that will attenuate enough radiation such that the low-energy portion of the spectrum will not dominate the matching algorithm. However, a thickness so great that eliminates most of the spectrum altogether is also not desirable. Making multiple measurements with different added filtration and using a least squares approach to average the multiple estimated spectra can increase the accuracy of the fitted spectrum, but will simultaneously add to the data collection effort.

2.5 Conclusion

We have developed a method to estimate the shape and thickness of materials representing the attenuation of shaped filters used in clinical CT scanners. The

method requires minimal equipment – a small ionization chamber and aluminum filters, and it involves relatively simple computational algorithms. The approach was tested in a laboratory and evaluated for an actual clinical system. Further collection of data from more clinical scanners and a comparison of radial dose profiles from simulations and experimental measurements are needed for additional verification.

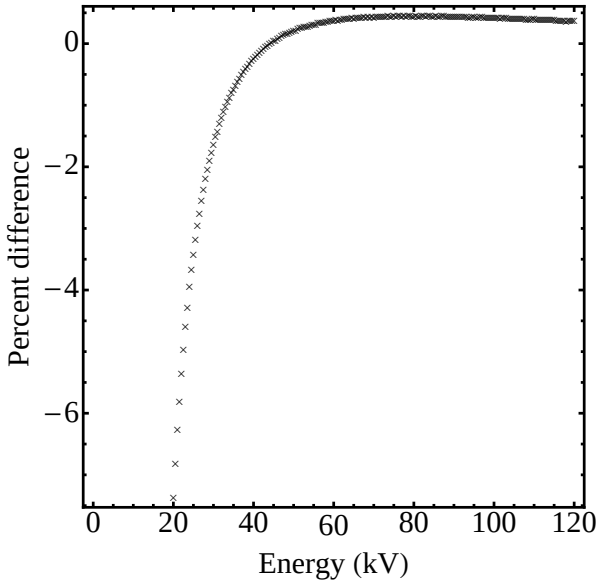

Figure 2.6: The percent difference in spectra resulting from a test filter with 3 mm Al and 20 mm PMMA and the calculated equivalent 3.16 mm Al and 18.75 mm PMMA.

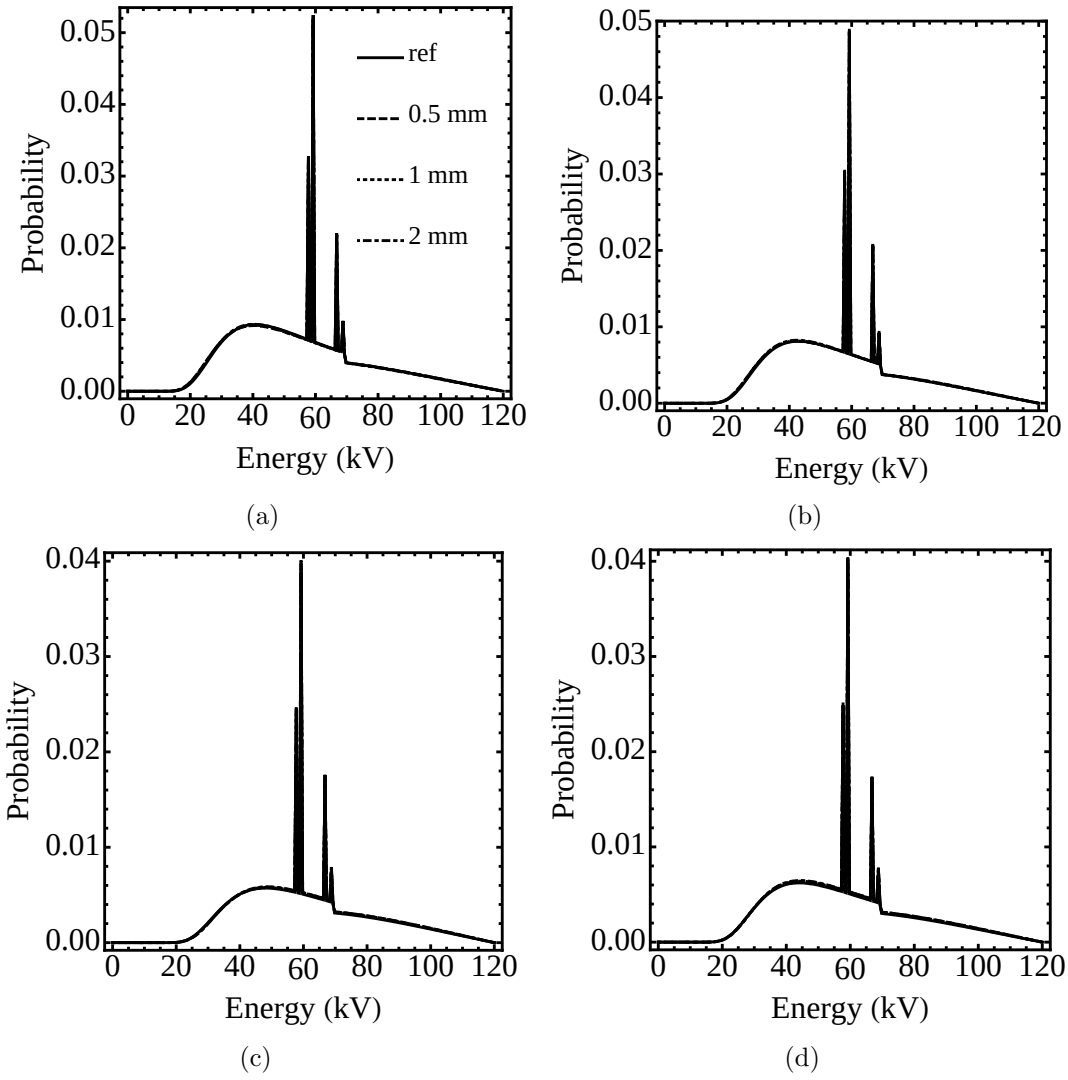

Figure 2.7: The spectra resulting from the unknown mAs algorithm. The measured test filters were: (a) 2 mm Al and 10 mm PMMA, (b) 3 mm Al and 10 mm PMMA, (c) 6 mm Al and 10 mm PMMA, and (d) 3 mm Al and 20 mm PMMA. In each plot there are four spectra - the reference expected spectrum (ref) from the known material thicknesses and the three spectra characterized using a different starting point in Figure 2.2. The spectra are normalized by the area of the spectrum in plot (a) such that a relative emission probability of photons by energy and "angle" was determined.

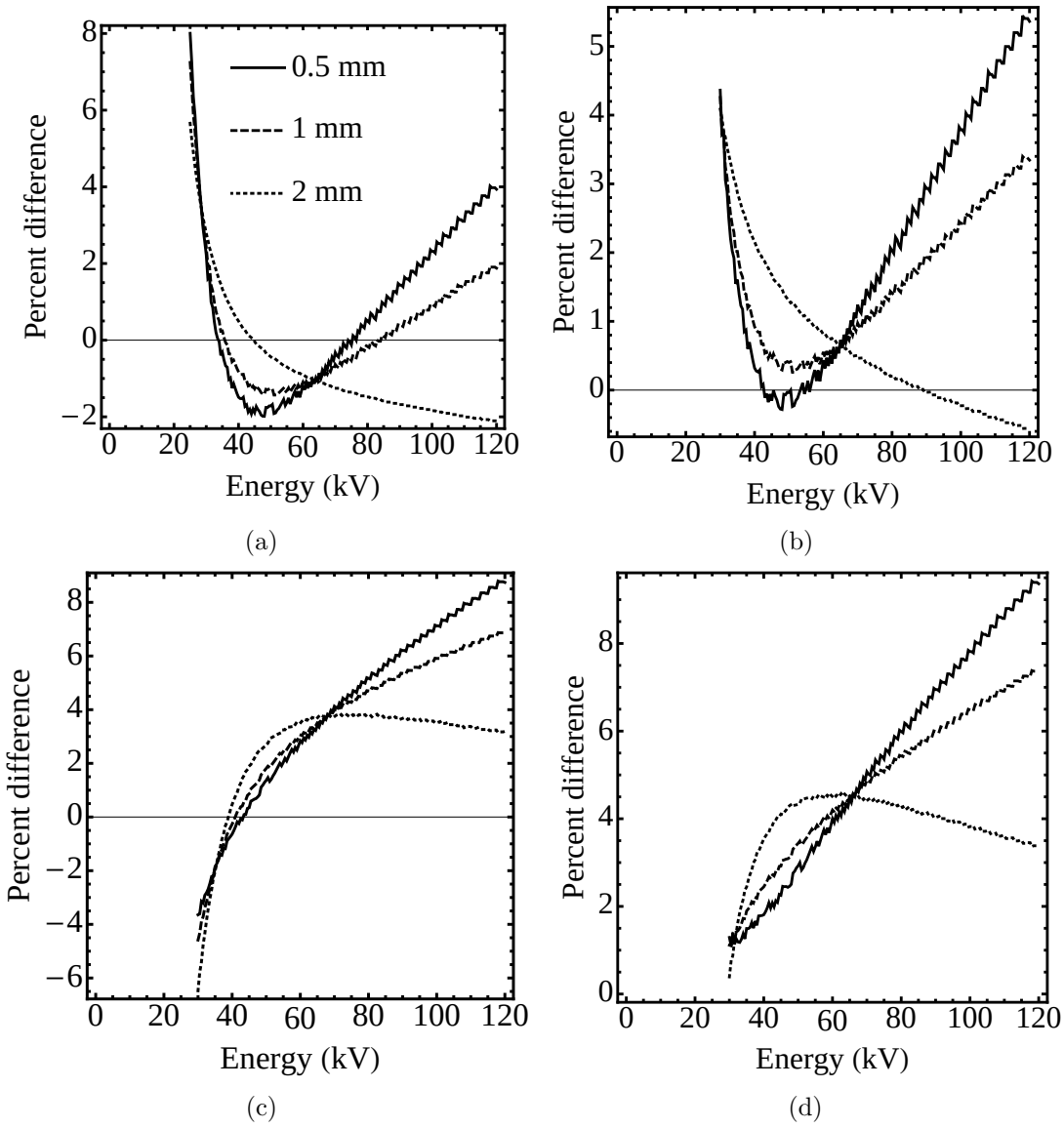

Figure 2.8: The percent difference among spectra calculated using the unknown mAs algorithm and assumed Al thickness in the first filter of 0.5, 1 , and 2 mm. The measured test filters were: (a) 2 mm Al and 10 mm PMMA, (b) 3 mm Al and 10 mm PMMA, (c) 6 mm Al and 10 mm PMMA, and (d) 3 mm Al and 20 mm PMMA.

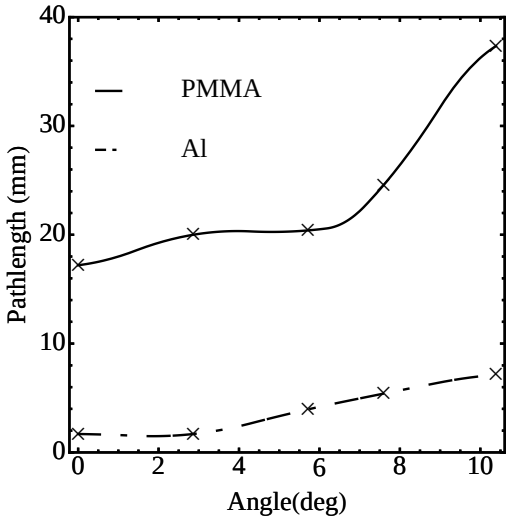

Figure 2.9: The angle dependent profiles of PMMA and Al calculated to comprise the attenuation-equivalent filtration of a Toshiba Aquilion 64 for a small field of view. The profiles were interpolated with second order splines fit to the algorithm-evaluated data points. PMMA is shown as a solid line, whereas aluminum is shown as a dashed line.

Chapter 3

Measuring Dose

3.1 Overview

3.1.1 CTDI metrics

The fundamental dose metric from which the most common modern CT dose metrics are defined is the Computed Tomography Dose Index.[56] CTDI is defined as:

$$CTDI = \frac{1}{nT} \int_{-\infty}^{\infty} D_1(z) dz, \tag{3.1}$$

where $D_1(z)$ is the dose as a function of position along the z axis coordinate for a single scan dose profile at a given point in the x and y plane, divided by the slice thickness T and number of images n, as stated by the manufacturer. The CTDI value represents the integral under the z-axis radiation dose profile of a single scan to produce 1 tomographic slice of the volume of interest. Measuring the pure CTDI is very time consuming, meaning it is rarely performed.

For this reason, a more convenient variant, the so-called CTDI_{100}, is now regularly used as a quality assurance measurement. It is defined by the International Electrotechnical Commission (IEC) and American Association of Physicists in Medicine (AAPM) as:

$$CTDI_{100} = \frac{1}{nT} \int_{-50mm}^{+50mm} D(z) dz, \tag{3.2}$$

using 100 mm active length pencil ionization chambers to measure the exposure along the central axis and at the periphery (1 cm below the surface) of polymethyl methacrylate (PMMA) cylindrical phantoms. A photograph of the instrumentation involved in collecting the $CTDI_{100}$ is shown in Figure 3.1.

3.2 Longitudinal Dose Profiles

3.2.1 Introduction

The advent of multislice computed tomography (MSCT) allows for faster imaging studies using wider x-ray beams.[33] The penalty paid for this ease of imaging is an increased exposure of the patient population to ionizing radiation.[30] Accurately characterizing radiation dose delivered to patients becomes a concern as the maximum beam width of some of these machines tends to become wider than the 100-mm charge-collection length of the pencil ionization chamber conventionally used in CT dosimetry to measure the computed tomography dose index ($CTDI_{100}$), the current dose metric.[13] Alternatives to the $CTDI_{100}$ evaluation have been suggested, including applications of a conventional ionization chamber[26] and using a larger phantom[48]. Dixon et al[26] suggest using a small ionization chamber and translating the phantom through the tomographic plane, in effect integrating the same amount of dose as would be collected by a stationary pencil chamber of length equal to the translation distance. While this method allows one to overcome the length limitation of the pencil chamber, the phantom must still be long enough to allow for the generation of a distribution of scatter radiation sufficiently broad to be

considered clinically relevant. In the present work we develop size specifications for the design of a cylindrical phantom that can be used for dose evaluation of CT scanners. Specifications are determined such that the phantom incurs approximately the same dose as would an infinitely long cylinder, but yet is of a size and weight that a person can carry. These determinations are made by simulating dose profiles in cylindrical phantoms using the PENELOPE Monte Carlo package.[54, 51] Additionally, we investigate a previously developed semi-empirical computational model that allows one to represent the dose profile corresponding to abeam of arbitrary width.

3.2.2 Methods

3.2.2.1 Simulated CT scanner

Fig. (3.2(a)) and (3.2(b)) shows the setup of the generic CT system used for the simulations. A two-dimensional detector was modeled. Due to the cylindrical symmetry of the phantom, only one projection is simulated, i.e. there was no modeling of multiple projections through a 360-degree rotation. The focal spot and detector plane are each separated from the isocenter by 60 cm. The phantom symmetry axes intercept the isocenter, and the axis of cylindrical symmetry is aligned along the axis of rotation of the scanner. In the simulations the beam originates from a focal spot modeled as a point source of rays collimated with lead (that is 100% attenuating), and this modeling allows for a variable beam width along the z-axis while limiting the x-axis width to the phantom diameter. Bow-tie shaping filtration was not modeled in the simulations.

3.2.2.2 Phantoms

The phantoms are modeled as polymethyl methacrylate (PMMA) cylinders described mathematically with quadric surfaces, of diameters 10, 16, 20, 24 and 32 cm in the xy-plane and lengths 15, 30 and 300 cm along the z-axis. For the purposes of these simulations, 300 cm is deemed to be sufficiently long such that the magnitude of the radiation-scatter tails of the dose spread function (DSF) at the extremities is essentially "zero". The diameters were chosen to reflect and expand on those currently in use for evaluation of dose. PMMA was selected because it is commonly used for the reasonably acceptable similitude of its attenuation proprties to that of human tissue and because it is a convenient medium for comparison to $CTDI_{100}$, as PMMA is required for conventional CT dosimetry in U.S. and international standards.[22] For dose evaluation, each cylinder was divided into energy-deposition sub-volumes comprised of concentric regions of 2 mm thickness. Along the z-axis, the cylinder was divided into 1 mm sections for most cases; but for the 10 micrometer beamwidth simulation the cylinder was divided into 0.03 mm sections along z.

3.2.2.3 Monte Carlo simulations

The PENELOPE[54, 51] Monte Carlo radiation transport code was used for all simulations in this study. The code has been extensively validated,[55] so direct validation was not performed here. A radiographic projection of each cylinder was created with an x-ray source was modeled as a cone beam (of the same cone angle

for all collimations) originating from a point focal spot at a source-to-cylindrical symmetry axis distance of 60 cm. Tube-current modulation was not modeled. The x-ray energy spectrum was provided in a look up table and was based on a 120-kVp source filtered with 3 mm thick aluminum (Fig. (3.2(c))). Beam width at the isocenter was varied among the following values at the isocenter: 0.01, 0.1, 1, 10, 20, 50, 100, 150, 200, 300, 400, 500, and 600 mm. A total of 1×10^9 incident photons were simulated for most projections, while 2×10^{10} photons were used for the 0.01 mm beam widths to reduce statistical uncertainty.

3.2.2.4 Determination of phantom lengths

For each diameter, the length of the phantom was chosen to be twice the distance from the maximum of the dose profile to its 5% level. This criterion establishes practicable design lengths of phantoms and, for scanning at any particular collimation, ensures that each phantom is long enough to incur neraly all of the dose that would be distributed along the length of an infinitely long cylinder.Establishing design lengths this way was done for each beam width for each phantom diameter.

3.2.2.5 Dose-profile reconstruction theory

The mathematical construction of dose profiles has been discussed at length previously[14], and so only the main points are summarized here. The dose profile of a given x-ray beam can be conceptualized in terms of two components - the contribution from primary scattering (that is, the spatial distribution of dose asso-

ciated with primary-photon-generated photoelectrons and Compton electrons) and the contribution from secondary scattering (photo- and Compton-electron energy deposition following transport of Compton and Rayleigh scattered secondary photons). While the dose profile can be reconstructed with sufficient knowledge of these components, the primary beam model can be very complicated, especially if one includes the heel effect and tilted anodes of clinical CT systems.[27] However, since the objective of our study is to broadly characterize how dose profiles are related to scattering-medium dimensions as a function of beam width, the heel effect and anode tilt are a second-order concern not incorporated in to the modeling.

In addition to explicit modeling of collimated ray geometry and Monte Carlo simulation of transport, we investigated the application of mathematical convolution as an alternative method to compute dose profiles.For this purpose we modeled the primary beam as a pulse of dimensionless unit height and width equal to the beam width at the isocenter. This function describes the source in an ideal way as a homogeneous, contiguous distribution of rays incident in effect perpendicular to the x-z plane, i.e. approximating primary photons incident on the phantom in parallel rays originating from a point inginitely far away.

The scatter model is developed by taking advantage of the shift invariance of scatter-radiation generation along the longitudinal axis of a uniform, cylindrical phantom.[9] A very-narrow-slit beam of primary radiation can be used to probe the local scatter response via Monte Carlo computation, and this response function can then be applied as the kernel of a convolution representation of the axial dose profile. Thus, with our simulation results and primary-beam model, a dose profile associated with

a beam of width w can be represented as a convolution (denoted the asterisk):

$$D(z) = a \times S(z) * H(z) \tag{3.3}$$

where dose profile $D(z)$ corresponds to the average dose incurred over the phantom circular cross section located at z, where $S(z)$ is the scatter kernel evaluated through Monte Carlo simulation, and where $H(z)$ represents the primary beam, mathematically described with a Heaviside function in first approximation:

$$\begin{aligned} H(z) &= 1, |z| < \frac{w}{2}, \\ H(z) &= 0, |z| > \frac{w}{2}, \end{aligned} \tag{3.4}$$

The coefficient a is a scaling factor that allows for comparisons to results of PENELOPE simulations or to those of experimental measurement.

3.2.3 Results

3.2.3.1 Dose profiles constructed via explicit modeling of collimated ray geometry and Monte Carlo simulation

The cross sectional average dose profiles in the 32 and 16 cm diameter phantoms obtained from direct Monte Carlo simulation, i.e. not involving the convolution of a scatter kernel and primary beam, are plotted in Fig. (3.3). These particular figures are representative of the plots corresponding to the other phantoms as well. Dose data were collected only within the phantoms and hence are not reported for values of z extending beyond phantom lengths. The scattered tails fall off asymptotically with distance from the primary-beam sections. In the 15 cm long phantoms,

the dose tends to saturate with increasing beam width much more quickly than in the longer phantoms. Moreover, the maximum value reached is lower than in the longer phantoms. These trends suggest that the scatter-radiation contribution that would otherwise accrue in longer phantoms is being lost beyond the 15-cm long phantom longitudinal bounds, which in turn implies that the dose values in this phantom do not scale with larger beam widths. The dose profiles associated with the 300 cm long phantoms provide insight into the approach to peak dose equilibrium, the condition in which the collimator is opened so wide that scatter radiation associated with rays incident through the collimator near its edges originates in the phantom too far away to make more than a negligibly small additional contribution to the peak dose. For the 32 cm diameter cylinder, the 15 cm long phantom reaches an equilibrium peak dose of 85% of that of the 300 cm long phantom, whereas the 30 cm long phantom reaches an equilibrium peak dose of 97% of the 300 cm long phantom. For the 16 cm diameter cylinder, the equilibrium peak doses of the 15 cm long and 30 cm long phantom are 92% and 99%, respectively, of that of the 300 cm long phantom.

3.2.3.2 Dose-length integral

The net loss of scattered radiation leaving finite-length phantoms through their surfaces affects not only the approach to equilibrium and the magnitude of the plateau of dose profile, but also dose-length integral that would be measured in a phantom. The ratios of dose-length integral (D_T) between the shorter cases ($D_{T,15}$, $D_{T,30}$) and long case ($D_{T,300}$) are summarized in Tables 3.1 and 3.2 for the

16 and 32 cm diameter phantoms, respectively. The results show that under these conditions, increasing beam width results in a growing discrepancy between the dose-length integrals for shorter cylinder vs. longer cylinder. In the 30 cm long phantom case, the ratio of dose-length integral stays relatively constant until the beam width begins approaches 15 cm, while in the 15 cm long phantom case the ratio of dose-length integral is relatively constant until the beam width approaches 5 cm. Even when the beam width is shorter than the phantom length, 8-12% of the dose-length integral associated with a 300-cm long phantom would not be registered by a 15 cm long phantom.

3.2.3.3 Phantom Design-Length Determination

The phantom design length is defined as twice the distance along z from the maximum of the dose profile to its 5% level. Results are plotted in Fig. (3.4) and they demonstrate that the scattered tail causes the dose profile to be much larger along the z axis than the primary beam width. Moreover, the range of the 5% maximum dose increases with increasing beam width. After an initial phase up to 8 cm beam widths, the length necessary to fully characterize the dose profile grows linearly with increasing beam width.

3.2.3.4 Scatter kernel

The scatter kernel is determined by simulating a very thin beam (in this case 10 μm), in the 300 cm long phantom. The output dose profile of this simulation

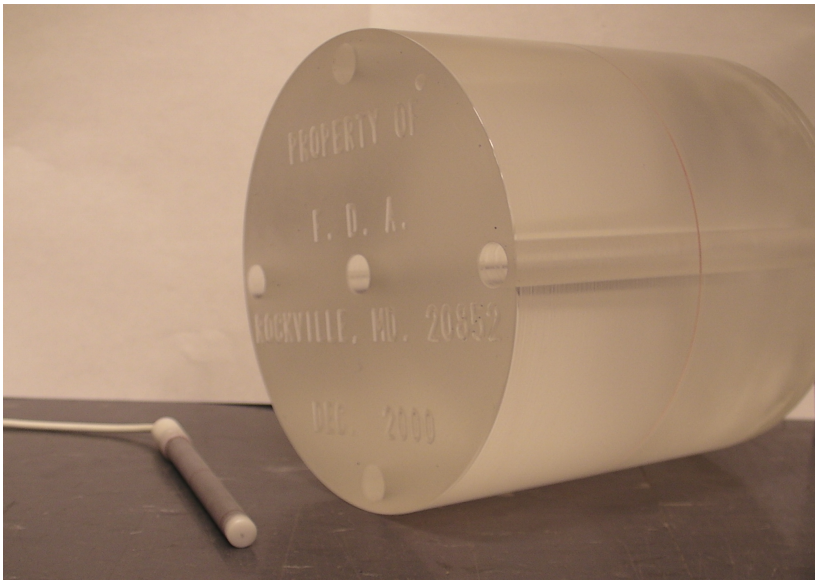

Figure 3.1: Instrumentation involved in the measurement of $CTDI_{100}$. Pictured is the 100 mm ionization chamber, and a 16 cm diameter head phantom. The ionization chamber is equipped with a sleeve to minimize the air gap when it is inserted into the measurement hole, and the holes not in use are plugged with PMMA rods to eliminate any air gaps.

Beam width (cm)	$D_{T,15}/D_{T,300}$	$D_{T,30}/D_{T,300}$
1	0.912	0.986
2	0.912	0.986
5	0.906	0.986
10	0.885	0.983
15	0.837	0.978
20	0.661	0.969
30	0.448	0.922
40	0.344	0.738
50	0.282	0.606
60	0.243	0.521

Table 3.1: Ratio of dose-length integral in 16 cm diameter phantoms between the 15 and 30 cm long cases and the 300 cm long case for given beam width.

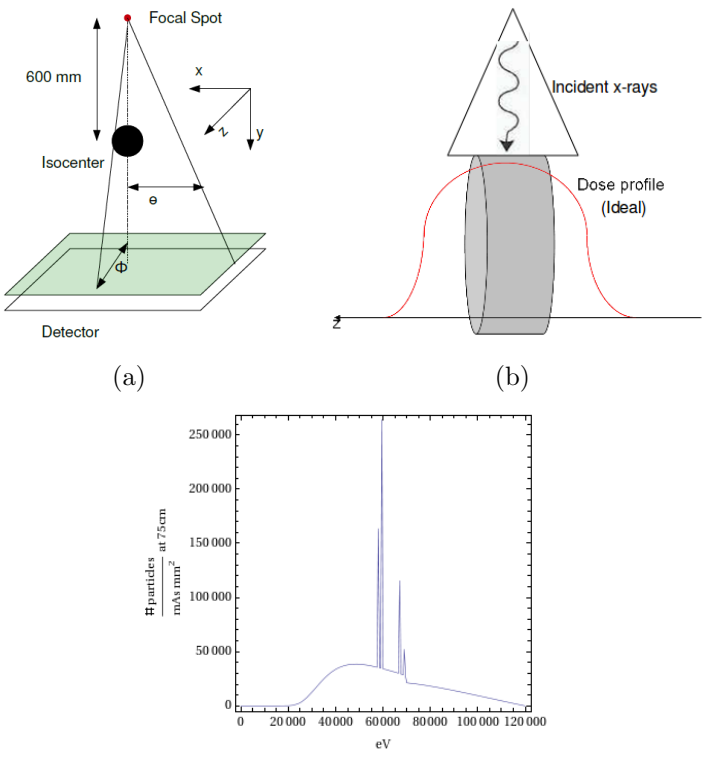

Figure 3.2: (a) Geometry of the simulated system. (b) Schematic representation of a phantom with dose profile superimposed. (c) X-ray spectrum simulated.

Beam width (cm)	$D_{T,15}/D_{T,300}$	$D_{T,30}/D_{T,300}$
1	0.837	0.965
2	0.836	0.965
5	0.831	0.964
10	0.813	0.960
15	0.776	0.953
20	0.674	0.943
30	0.457	0.904
40	0.351	0.788
50	0.289	0.649
60	0.250	0.560

Table 3.2: Ratio of dose-length integral in 32 cm diameter phantoms between the 15 and 30 cm long cases and the 300 cm long case for given beam width.

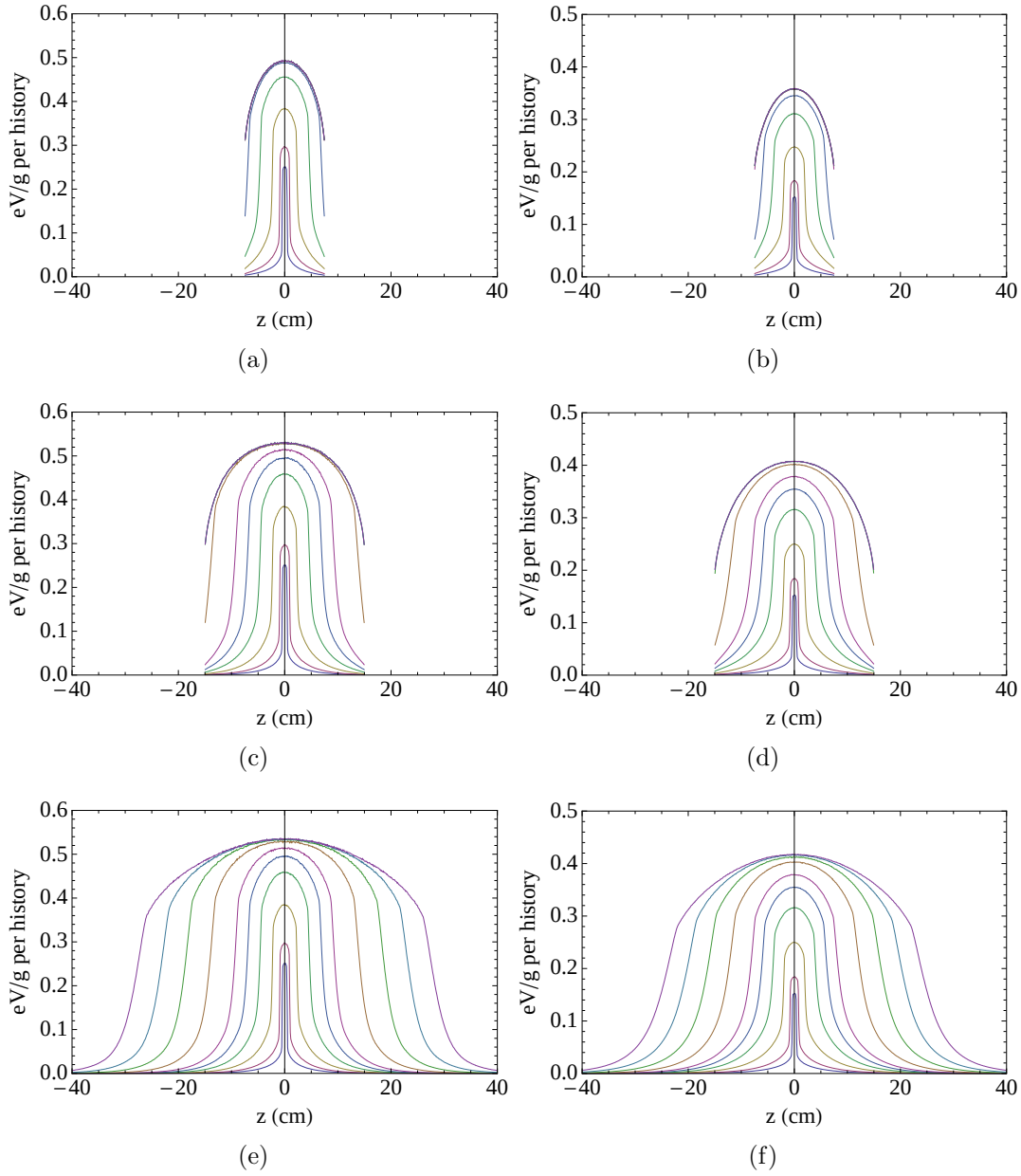

Figure 3.3: Cross-sectional average energy deposited per unit mass per incident-photon history along z-axis of PMMA cylinders. In the left column the phantom has a diameter of 16 cm and in the right column 32 cm. The phantom lengths are 15 cm in the first row, 30 cm in the second row and 300 cm in the third row. The beamwidths corresponding to each curve (from smallest to largest) are 1, 2, 5, 10, 15, 20, 30, 40, 50 and 60 cm.

is taken to be the scatter response for the given system. The scatter kernel is normalized by area, such that integrated dose is 1 dimensionless unit. This is shown in Fig. (3.5). The figure shown is the scatter response from the 16 cm diameter cylinder, and it is representative of those from other diameter phantoms as well. The extent of these curves along the central axis was selected so as to not limit the reconstruction of the dose profile via convolving - i.e. these values are large enough so that the scatter contribution a large distance z from the primaries was approximately zero.

3.2.3.5 Dose profiles via convolution

Applying the results of the previous section and Eqs. 3.3 and 3.4, we constructed convolution-derived dose profiles with beam widths varying from 1 to 60 cm (Fig. (3.6)). These plots should correspond to Fig. (3.3) (e) and (f). Qualitatively, the curves differ in shape at the shoulders. For direct comparison, some of the convolution-derived dose profiles for the 16 cm diameter phantom are compared in Fig. (3.7) to those obtained by direct Monte Carlo simulation. Differences in peak dose values (including results not shown in Fig. (3.7)) do not exceed 3%. Differences in dose-length integrals range between 5 and 7%.

3.2.4 Discussion

In order to design phantoms that would reasonably represent the build-up and distribution of dose incurred in patients of computed tomography, we used Monte

Carlo techniques to estimate dose profiles as a function of beam width and phantom diameter. The resulting design lengths suggest that for the relatively wide beam widths associated with MSCT, phantoms longer than 14 to 15 cm long phantoms currently used in CT dosimetry are necessary to include most of the contribution from scatter radiation. However, when cylinders with smaller diameters are considered, shorter lengths are possible. For the current generation of scanners with z-axis coverage of 4 to 8 cm, the 16 and 32 cm phantoms require design lengths between 20 and 30 cm. The findings in Tables 3.1 and 3.2 support the idea of designing relatively longer phantoms for more accurate dosimetry: dose-length integrals are approximately constant until the beam width exceeds a threshold value. When the beam width exceeds such a threshold, the phantom is insufficiently long to generate the spatial disposition of scatter energy that would occur in a patient, and some of these contributions to the dose-length integral are lost. Such losses occur when beams incident on 15 to 30 cm long phantoms exceed widths between 15 and 20 cm. Fig. (3.4) suggests a slope (phantom length/beam width) of 0.93 for the 16 cm diameter phantom and 0.87 for the 32 cm diameter phantom, values which imply phantom masses of over 60 kg for very wide beams.

While phantoms that heavy argue against the prospect of their widespread use, convolution-based construction of dose profiles suggests a potentially more practicable alternative. Our results demonstrate that dose profiles reasonably similar to those derived from direct Monte Carlo simulation of suitably-modeled beam-phantom irradiation geometry can be constructed from a Monte Carlo-simulated scatter kernel convoluted with a simple model of the primary beam as a box func-

tion appropriately normalized to the actual magnitude of emissions from a scanner. To estimate the height of this box function, one could insert filtration equivalent to that of the phantom PMMA and air between the source and a small ionization chamber. Measuring the dose in air at this point gives the height of the primary input function. The dose profile for any particular beam width can be estimated by means of such convolution, and it would approximately represent actual dose profile so long as the simulation used to construct the scatter kernel matches the actual scatter for such a system.

This convolution-based approach would reduce the amount of bulky equipment a medical physicist would need to carry in the clinical setting for quality assurance measurements. Limitations of the convolution construction include a systemic overestimation of dose associated with the modeling of the primary beam. A geometric argument can be made, especially for larger beam widths, that the incident beam is not comprised of parallel rays. Acutely-angled rays traveling through the phantom then would involve irradiating areas non-uniformly in the x-y and x-z planes. Under such circumstances, one would expect to see a smoothing out of the dose profile shoulders with respect to those evident in the results associated with our simplistic model of primary beam, which is exactly what is seen in the more completely modeled Monte Carlo simulation results. One could refine the simple model of the primary beam with geometric adjustment factors. For example, a cosine or trapezoidal function would be starting points, and one could then approach the complexity of the model of Dixon et al.[27] Kyprianou demonstrated how to ray-trace a cylinder to extract a primary function.[45] While this approach also assumes parallel

rays, it should also be better than that of a box function. Finally, this convolution method is also limited by the ability to realistically simulate output of actual CT scanners used clinically. A conversion factor between Monte Carlo simulations and clinical CT systems is needed (e.g., either by normalizing measurements with respect to the same simulation dose in air or by calculating a conversion factor relating the number of specific histories to the mAs for each system).

3.2.5 Remarks

We examined two alternative methods for MSCT dosimetry and have shown that the approach using longer phantoms is relatively more accurate, but limited in practicality by the sizes and weights that would be involved. The convolution-based approach would be practical and simple to implement, but the accuracy of this method is not yet sufficient for quality-assurance purposes.

3.3 Radial Dose Profiles

3.3.1 Introduction

The proliferation of third generation CT scanners in the late 1970s necessitated a reliable and reproducible method for reporting radiation exposure or dose delivered by those systems. One such metric was the Computed Tomography Dose Index (CTDI).[56] A variant of the $CTDI_{100}$, the weighted value of CTDI ($CTDI_w$), is defined as

$$CTDI_w = \frac{1}{3}CTDI_c + \frac{2}{3}CTDI_p, \tag{3.5}$$

where $CTDI_c$ and $CTDI_p$ denote the CTDI at the center and periphery of the phantom, respectively.

Recently, the ability of the CTDI metric to reflect dose to patients undergoing CT imaging in systems with larger beamwidths has been questioned.[13, 26, 48] Some have looked at the efficiency of the $CTDI_{100}$ with increasing beamwidths, finding that the efficiency falls as the beamwidth exceeds the charge collection length, but is relatively flat when the beamwidth is smaller than the charge collection length.[13] Others have looked using a shorter ionization chamber or a longer phantom when making measurements of dose to increase the efficiency of $CTDI_{100}$ or replace it with another metric altogether.[26, 48] Another work chose to examine the selection of weighting factors in the $CTDI_w$ using geometrically formulated arguments.[8] This approach argues that the central axis dose is underrepresented in the current $CTDI_w$, and that other weighting factors should be used.

We have previously used Monte Carlo simulations to investigate the dose profiles along the longitudinal axis of cylindrical phantoms.[5] The primary purpose of this work is to investigate dose profiles in the radial (or axial) plane of a cylindrical phantom. We perform a range of simulations to report the relationship between $CTDI_w$ and the total energy deposited in the phantom. The dose profiles versus radial distance from the center of the phantom are examined to gain insight into the weighting factors used in $CTDI_w$. Finally, we investigate the effect of the diameter of the phantom on the radial behavior of the dose profile.

3.3.2 Methods

The phantoms were modeled as polymethyl methacrylate (PMMA) cylinders described mathematically with quadric surfaces, of diameters 16 and 32 cm in the xy-plane and length 300 cm along the z-axis (see Fig 3.8). For the purposes of these simulations, 300 cm was deemed to be sufficiently long such that the magnitude of the radiation-scatter tails of the dose spread function (DSF) at the extremities was essentially "zero." PMMA was selected because it is commonly used for the reasonably acceptable similitude of its attenuation proprties to that of human tissue and because it is a convenient medium for comparison to $CTDI_{100}$, as PMMA is required for conventional CT dosimetry in U.S. and international standards.[22] For dose evaluation, each cylinder was divided into energy-deposition sub-volumes comprised of concentric annular regions of 1 cm thickness. Along the z-axis, the cylinder was divided into 1 mm sections along z. In addition to the concentric rings, dose was recorded to two CTDI-like regions-of-interest. These were two 10 cm long rods with diameter 1 cm within the phantom. They were located at the center, modeling $CTDI_{100,c}$, and the periphery, modeling $CTDI_{100,p}$, of the phantom (see Fig 3.9). The periphery region of interest was positioned such that the symmetry axis of the rod was 1 cm below the surface of the phantom.

The PENELOPE[54, 51] Monte Carlo radiation transport code was used for all simulations in this study. 360 radiographic projections (rotated 1 degree for each projection) of the cylinders were created with an x-ray source modeled as a cone beam (of the same cone angle for all collimations) originating from a point

focal spot at a source-to-cylindrical symmetry axis distance of 60 cm. The x-ray energy spectrum was provided in a look up table and was based on a 120-kVp source filtered with 3 mm thick aluminum. Beam width at the isocenter was varied among the following values: 1, 5, 10, 15, and 20 cm. A total of 1×10^8 incident photons was simulated for each projection, resulting in uncertainties (defined as two standard deviations) of less than 1 percent.

3.3.2.1 Laboratory calibration and verification

Our Monte Carlo simulations results are tabulated in values per history. In order to convert these values to per mAs, we devised a simple experiment. Using published KERMA conversion factors, we calculated the KERMA expected from our simulated spectrum in mGy per mAs.[24] We then ran a Monte Carlo experiment under the same conditions, with the results in mGy per history. Division gave us a conversion factor (specific to these conditions) of histories per mAs.

To validate that our results were reasonable, we constructed a cylindrical phantom with diameter 16 cm and length 45 cm. A hole with 1 cm diameter was drilled in this phantom parallel along the long axis of symmetry at the center. 1 cm tall plugs that fit the hole were also constructed. The phantom was placed on a stage 60 cm from an X-ray tube (a Varian B180 with an inherent filtration of 1 mm Al with 0.3 and 0.6 mm nominal focal spots) with 2 mm Al additional filtration. A Radcal model 9010 radiation monitor with a 0.6 cm^3 ionization chamber (Radcal Corp., Monrovia, CA) was placed at the bottom of the center hole. The phantom

was rotated through 360 degrees with 30 total exposures as dose was collected. Following the 360 degree rotation, the ionization chamber was removed, a 1 cm tall plug was placed in the center hole, and the ionization chamber was reinserted. Following each rotation of data collection, another 1 cm plug was inserted and thus a z-axis dose profile at 1 cm intervals was recorded. This experiment was modeled in our Monte Carlo simulation, and a continuous curve of dose along z was tabulated. The Monte Carlo results were converted to mGy per mAs using the technique described above. Because the ionization chamber was of a defined size, and also the possibility of imperfect positioning, the experimental measurement was actually the dose profile convolved with a 2 cm wide, off-center box function. For this reason, the simulated data was convolved with a 2 cm wide, off-center box before comparison with the experimental data. The degree of the offset of the convolution kernel was determined using iteration and minimization of the mean absolute percent difference between the simulated curve and experimental data.

3.3.2.2 $CTDI_w$ versus total energy deposited in the phantom

The dose delivered to each of the two ROIs was estimated for each projection angle. The sum of all 360 doses for each ROI was taken to be a $CTDI_{100}$-like measurement for a single axial rotation of the source at the center of the phantom, i.e. the $CTDI_{100,c}$ and $CTDI_{100,p}$. $CTDI_w$ was then calculated according to Equation 3.5.

Total energy deposited in the phantom was also estimated. Total energy was

used instead of dose as dose is dependent on the size of the phantom (a larger phantom would result in a "smaller" dose because of division by a larger volume). The ratio of $CTDI_w$ to total energy deposition was calculated for each beam width simulated and examined for trends. Additionally, different weighting factor sets were used to calculate other $CTDI_w$s to examine the effect of weighting factor choice.

3.3.2.3 Radial profiles of dose

Dose deposition was recorded within the 32 cm diameter phantom in bins divided radially (concentric annular rings) and along the z-axis, as described above. Because of the symmetry of the annular rings, dose was collected for one projection only. The dose estimates were plotted for each simulated beam width, and fitting functions were tested. The fitted functions were used to examine possible changes to the weighting factors in Equation 3.5.

3.3.2.4 Influence of phantom size on radial profile

The experiment described in section 3.3.2.3 was repeated with a 16 cm diameter phantom. The shape of the radial dependence of the dose profile was compared to that from the 32 cm diameter phantom. The differences in radial dependence of dose for different diameter phantoms are reported.

3.3.3 Results

All simulations were run on nodes of a supercomputer cluster, requiring approximately 2 hours of run time per projection.

3.3.3.1 Laboratory verification

The calibrated Monte Carlo results and the laboratory measurements for the center hole is shown in Figure 3.10. The experimental data points match well with the simulated curve. Minimizing the mean absolute percent difference between the two revealed a positioning error in the experiment of 0.52 cm, with a mean absolute percent difference of 9%. The manufacturer of the ionization chamber states a calibration uncertainty of 4% and energy dependence of 5%. Taking these values into account with possible alignment errors means it is reasonable to assume a good match.

3.3.3.2 $CTDI_w$ versus total energy deposited in the phantom

The dose to the ROIs versus projection angle is shown in Figures 3.11 and 3.12. The dose to the periphery shows sinusoidal behavior, while the dose to the center is flat, as expected. The average of the data points in Figures 3.11 and 3.12 represent the $CTDI_{100,p}$ and $CTDI_{100,c}$, respectively.

The ratio of $CTDI_w$ to total energy deposited versus beamwidth is shown in Figure 3.13. $CTDI_w$ is in units of mGy per mAs, and total dose is in units of Joules per mAs, therefore the ratio calculated here is in units of inverse kilograms, but

this is not taken to mean that it depends on the mass of the phantom. The ratio stays flat until the beam width begins to exceed the length of the ROI, which in the clinical setting would correspond to a beam width longer than the charge collection length of the ionization chamber. On the same plot, the ratio is shown for two other sets of weighting factors. The curves have the same shape, but are of differing magnitude.

3.3.3.3 Radial profiles of dose

The experiment described in section 3.3.2.3 resulted in a dose profile in two (cylindrical) dimensions: r and z. For visualization of general trends, contour plots of dose versus radius and z-location are shown in Figure 3.14. Plots of dose vs. radius at certain z-axis locations for each simulated beam width are shown in Figure 3.15 corresponding to the dashed lines superimposed on the plots in Figure 3.14. The dose curves do not show behavior that follows a straight line fit. In fact, a linear least-squares fit resulted in a coefficient of determination under 0.85. Rather, in the regions within the primary irradiation zone, the curves are fit much better by a polynomial. Through iteration of least-squares-fit with polynomials of increasing order, it was found that the coefficient of variation of the fit plateaued with a third order polynomial. However, even with a second order polynomial, the coefficient of determination of the fit was over 0.995. In the transition regions where z-location shifted from inside to outside of the primary irradiation beam, the behavior of the dose profile versus radius was much less predictable. As z-location deviated further

from the center of the beam, the dose closer to the periphery was the first to fall, resulting in a flattening of the curve. At z-locations outside the primary beam width, the radial shape of the dose profile became essentially flat, though still non-zero. The behavior with changing z-locations in this region is analogous to the results discussed in a previous work.[5] The peak dose at the center and periphery did not behave in the same ways with increasing beam width. The peak dose at the periphery increased with beam width until reaching a plateau when beam width equaled 15cm. The peak dose at the center did not reach a plateau within the beam widths simulated. This behavior fits with a previous discussion of the scatter kernel at different r-locations.[13]

3.3.3.4 Influence of phantom size on radial profile

The same experiment as above was repeated with a cylinder of diamter 16 cm. The results are shown in Figures 3.16 and 3.17. The r-dependence of the dose profiles remained more accurately modeled by a polynomial than a linear fit (coefficients of determination of 0.996 and 0.9, respectively). With z-locations that deviated from the center of the irradiating beam, the dose profiles exhibit the same "peeling off" behavior noted for the larger diameter phantoms.

3.3.4 Discussion

The first goal of this work was to examine the relationship between $CTDI_w$ and the total amount of energy deposited in the phantom. In figure 3.13 it was

shown that the ratio of $CTDI_w$ to energy deposited stayed constant until the beam width exceeds the length of the CTDI-like regions of interest. The shape of these curves follows closely the plots of $CTDI_{100}$ efficiency previously published.[13] The question that naturally follows is: what influence do the weighting factors have on this curve? It has previously been argued that the reason the $CTDI_{100}$ efficiency does not fall off more precipitously with beam widths between 1 and 10 cm is due to the changing nature of the dose profile. While, at increased beam width, more scattered radiation does not fall within the CTDI-like region, there is more overall radiation deposited from primary radiation in this region. It is believed that this counterbalance of effects leads to the stability of the CTDI metrics at smaller beam widths.[13] Due to the similar nature of the scatter tails along z at the center and periphery (as seen in Figure 3.15) it was expected that varying the coefficients in the $CTDI_w$ equation will not have a large effect on the shape of the ratio curve. However, because the $CTDI_{100,p}$ is larger in magnitude than $CTDI_{100,c}$, it was also expected that changing the coefficients would effect the magnitude of the ratio curve. Indeed, this was found to be the case as shown in Figure 3.13.

With this in mind, the next goal was to determine what the weighting factors should be to estimate the total dose to the phantom. If one has knowledge of the radial profile of the dose deposition in the cylinder, then the average dose to the whole cylinder is:

$$D_T = \frac{\int_0^R D(r)dr}{\int_0^R dr}, \tag{3.6}$$

Where R is the radius of the cylinder, and $D(r)$ is the dose profile in versus radial

postion. This is a cross-sectional average of the dose in the cylinder, and the denominator is necessary to keep units consistent when taking a spatial average. If we assume the dose profile is linear with respect to radius, then after integration and simple arithmetic, the resulting weighting factors are both 1/2, the same as proposed in other work.[8] Inclusion of a bow-tie-shaping filter in the CT system might result in a more linear radial dose profile, but this is not necessarily the case for all systems (e.g. cone beam/flat panel based systems). In the absence of a bow-tie-shaping filter, we have shown that the dose profile is more akin to a quadratic polynomial. Fitting a quadratic polynomial to the dose curve requires at minimum three measurement points. After introducing a third measurement point (the CTDI_m from the AAPM body phantom, for example) integrating Equation 3.6 and solving the three simultaneous equations results in a much more complicated formula for dose:

$$D_T = \frac{R_p(CTDI_{100,p}R_m(3R_m - 2R_p) - CTDI_{100,m}R_p^2 + CTDI_{100,c}(3R_m^2 - 4R_mR_p + R_p^2))}{6R_m(R_m - R_p)}, \tag{3.7}$$

with R_p and R_m being the radial location of the periphery and middle holes, respectively.

Dose profiles in the radial direction are not always linear, and a quadratic fit forces the inclusion of a third measuring point and more complicated weighting factors. It is therefore reasonable to ask if there are other ways to use the same data. If using the CTDI_w as a QA/QC measurement, it might be more useful to report the periphery and center doses individually. This is because in the QA/QC

setting, the CTDI measurements are used to verify two things: the total energy output of the scanner, and the performance of the bow-tie-shaping filter. In this setting, relative doses are used to inform the operator about the function of the filter, while the absolute values of the doses inform about the scanner's total energy output. For shorter scan lengths, we have shown that one could use $CTDI_w$ as a proxy for total energy deposited, as the ratio between the two states constant until beam widths exceed 10 cm. A further advantage of reporting two values is in estimating the patient's skin dose. It is reasonable to assume that the $CTDI_{100,p}$ is a better indicator of skin dose than $CTDI_{100,c}$ or $CTDI_w$.

What is not addressed in this work is the relationship between these measures and risks of interest in the health care setting, such as patient dose or effective dose. While it was postulated that $CTDI_{100,p}$ might be a better indicator of skin dose that the other measurements investigated here, a direct relationship between $CTDI_{100,p}$ and skin dose was not examined. In order for these values to be useful in that setting, the relationship between deterministic or stochastic effects and these values must be investigated. Additionally, though the effect of the bow-tie filter on radial dose profiles was speculated at, it was not directly simulated.

3.3.5 Conclusion

It was shown that for current clinical CT scanners, the $CTDI_w$ is a measurement that will stably reflect the total dose to the cylindrical PMMA phantom. Further, the weighting factors necessary for the $CTDI_w$ to reflect the average total

dose to the phantom were calculated based on two radial dose profiles: linear and quadratic. We conclude the the $CTDI_w$ is a robust engineering QA/QC metric, but more investigation is needed regarding health care metrics for tracking dose and risk for patients undergoing procedures.

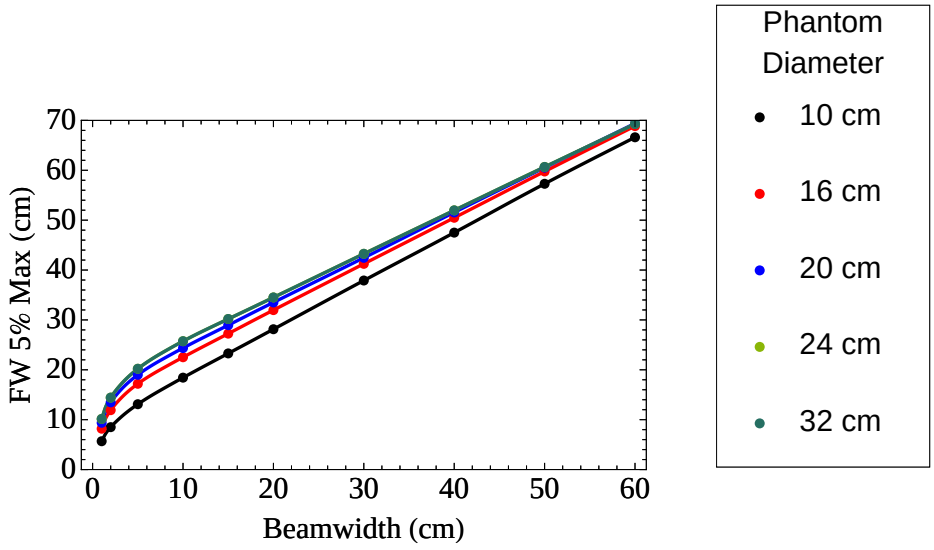

Figure 3.4: Length required to integrate energy deposition values greater than 5 % of maximum for given phantom diameter. The trend lines are second order interpolations.

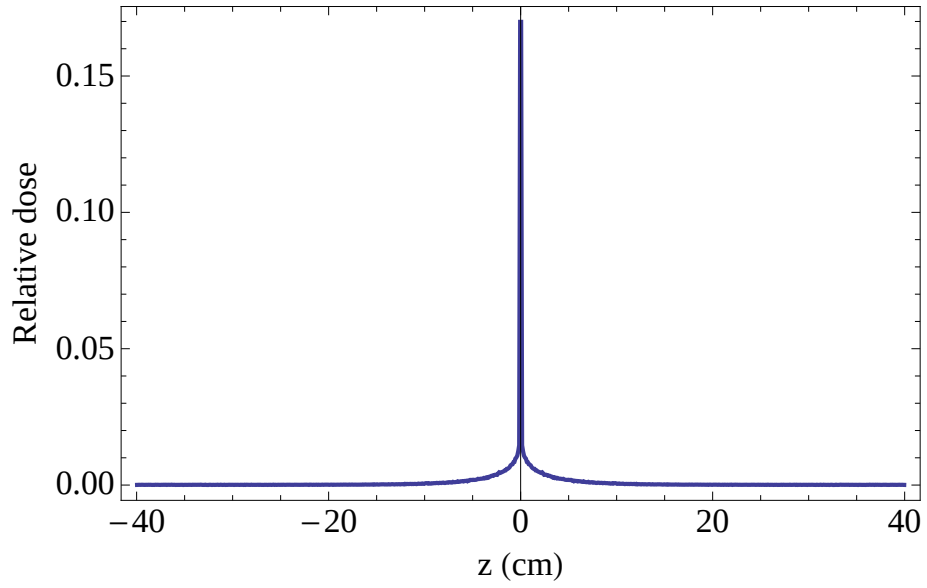

(a)

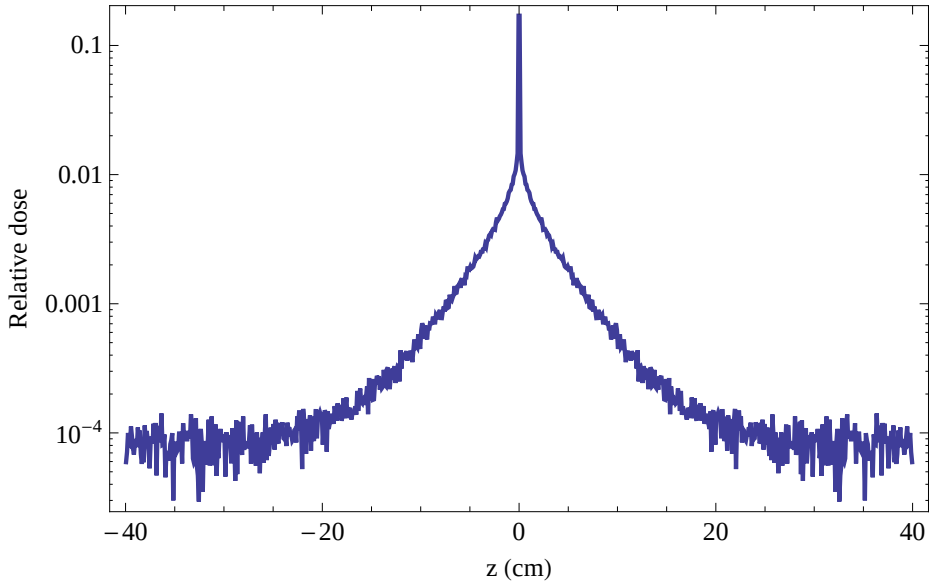

(b)

Figure 3.5: Scatter dose profile for 16 cm diameter, 300 cm long phantom (a) in linear scale and (b) in logarithmic scale. These plots are normalized to unit area and are representative of those of the other diameter phantoms.

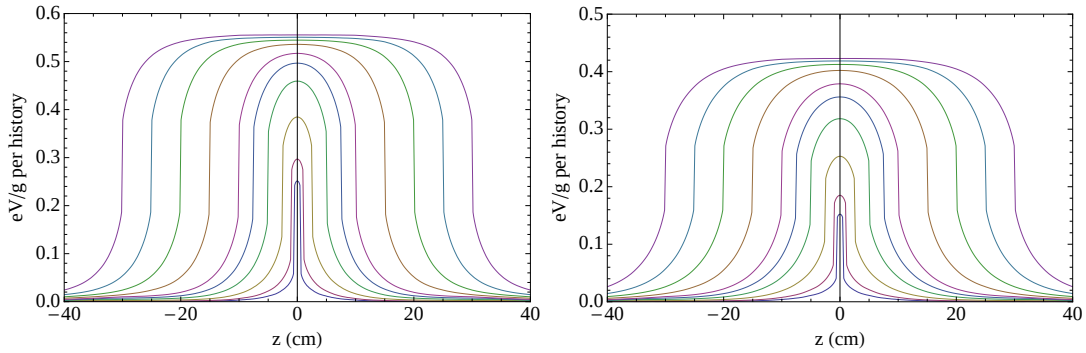

Figure 3.6: Dose profiles in the (a) 16 and (b) 32 cm diameter phantoms. These plots are comparable to those of Fig. (3.3) (e) and (f). The primary-radiation beam widths corresponding to the curves from smallest to largest are 1, 2, 5, 10, 15, 20, 30, 40, 50 and 60 cm.

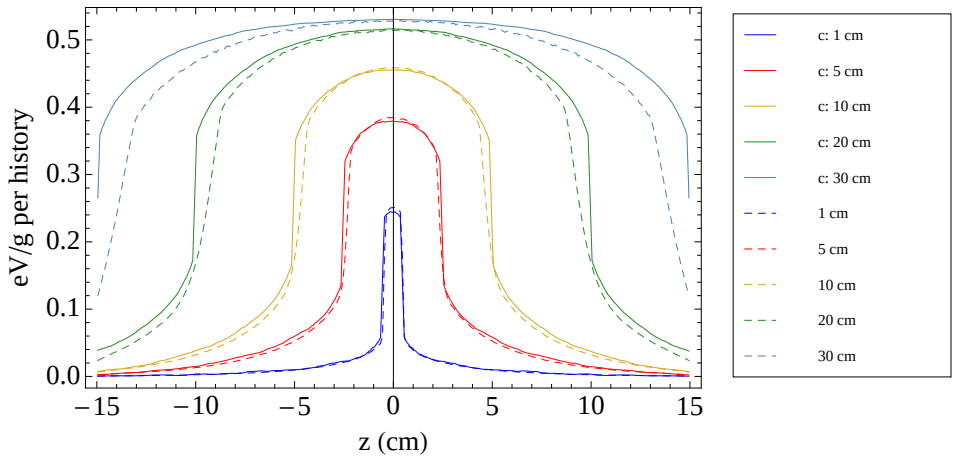

Figure 3.7: Dose profiles in the 16 cm diameter phantom as obtained through convolution (solid lines) and through direct simulation (dashed lines).

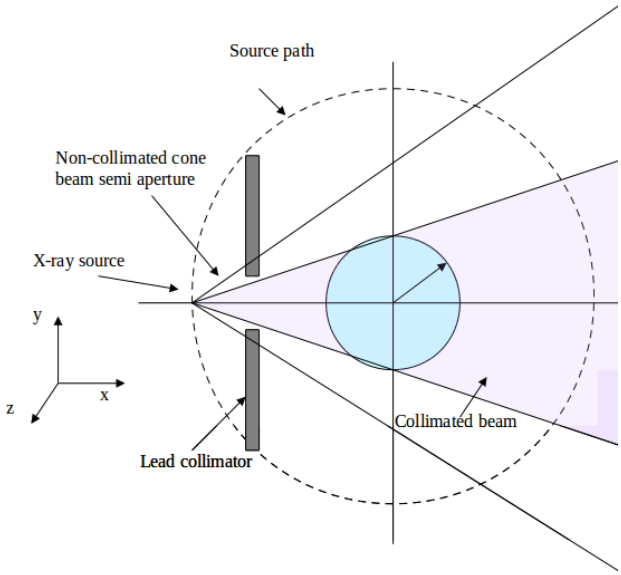

(a)

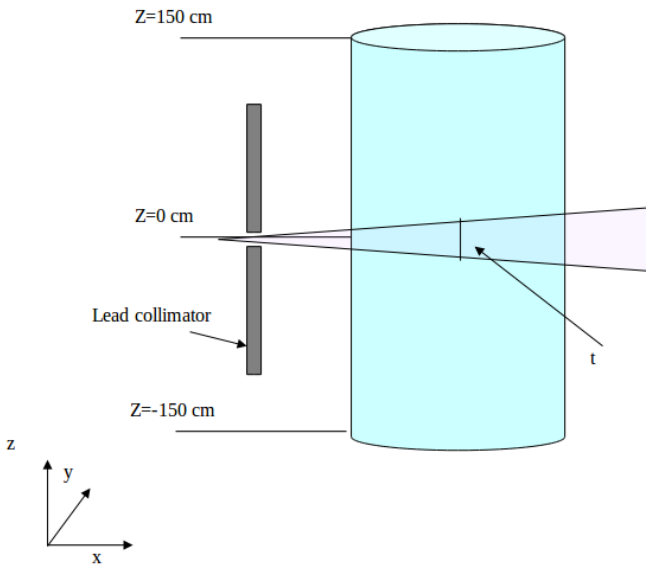

(b)

Figure 3.8: Schematics representing the modeled experiment. The PMMA phantom is 300 cm long in the z-axis, and a collimated x-ray source rotates about it 360 degrees. Thickness t is the beamwidth at the isocenter.

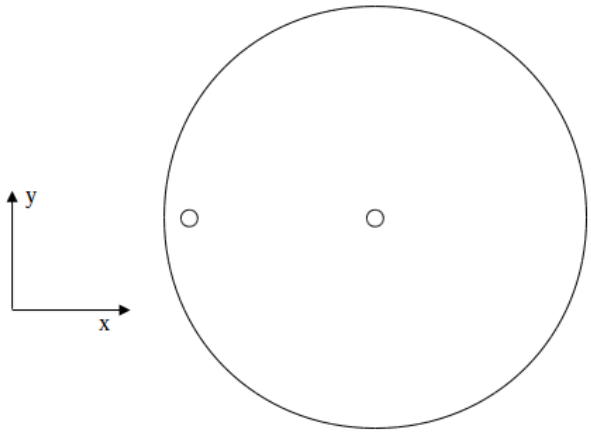

(a)

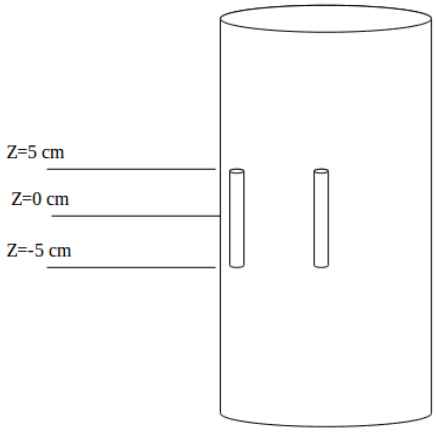

(b)

Figure 3.9: Depictions of the CTDI-like regions of interest. There are two CTDI-like ROIs where the dose is recorded - in the center and at the periphery. They are 10 cm along the z-axis, with diameter 1 cm. The center of the periphery ROI is located 1 cm below the surface of the phantom.

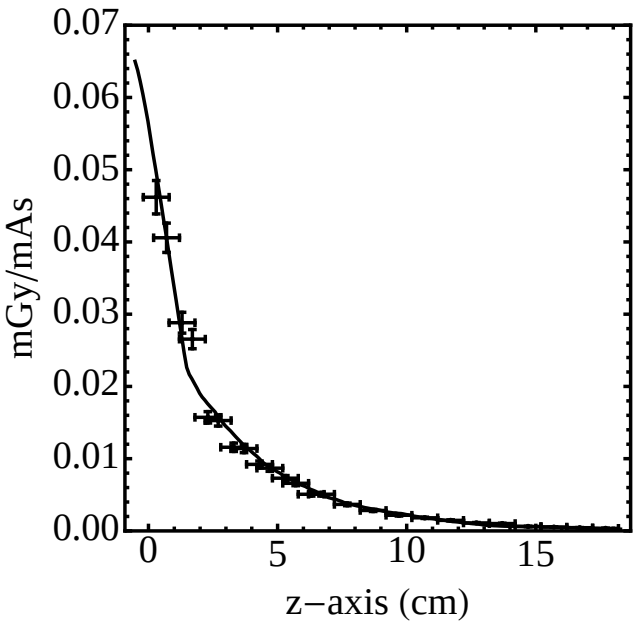

Figure 3.10: Comparison of experimentally measured vs. simulated z-axis dose profiles at the center of the phantom. The data collected in the simulation were continuous, and so were convolved with a *rect* function the size of the ionization chamber to get results comparable to experimental measurement. The solid line represents the simulated data after being convolved. The errors on the experimentally measured data are 5% along the y-axis (manufacturers stated uncertainty) and 0.5 cm along the z-axis (uncertainty in placement of ionization chamber).

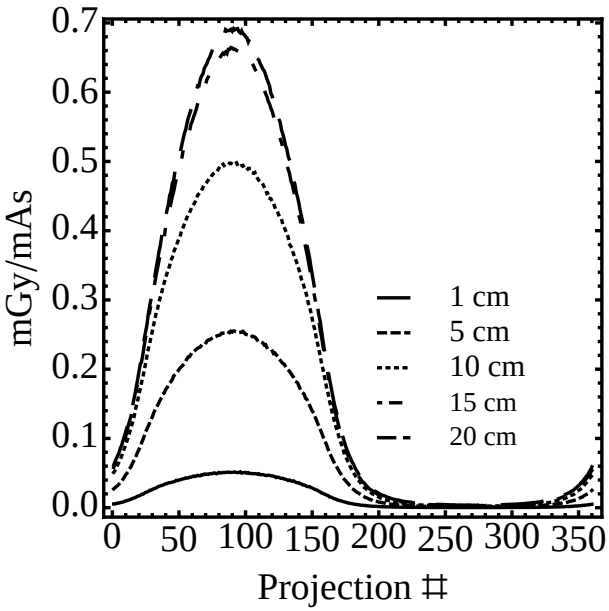

Figure 3.11: Dose to the periphery CTDI-like ROI vs. projection angle for five different beam widths. The order of beam widths from bottom to top is: 1cm, 5 cm, 10 cm, 15 cm, 20 cm. As expected, the dose vs. projection angle is sinusoidal and increases with increasing beam width.

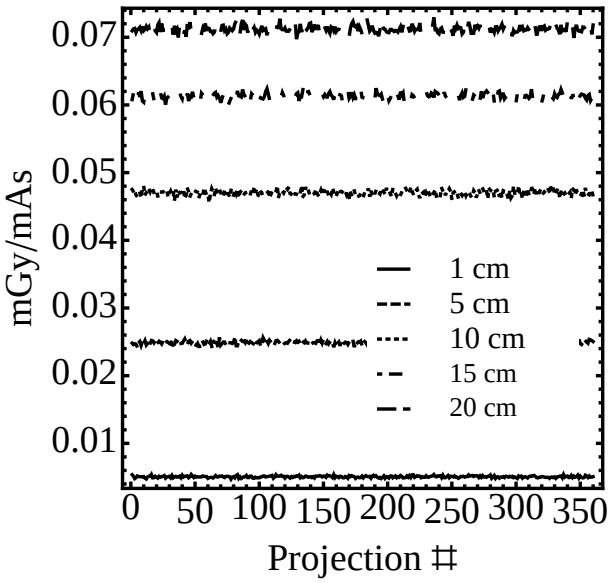

Figure 3.12: Dose to the center CTDI-like ROI vs. projection angle for five different beam widths. The order of beam widths from bottom to top is: 1cm, 5 cm, 10 cm, 15 cm, 20 cm. As expected, the dose vs. projection angle is flat and increases with increasing beam width.

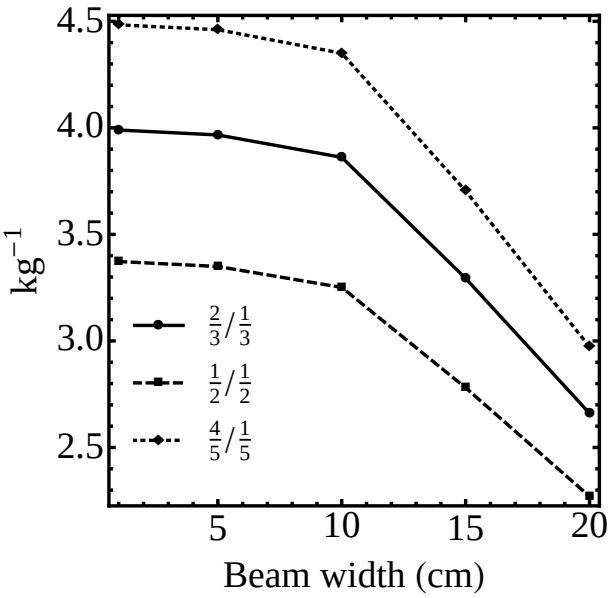

Figure 3.13: Ratio of CTDI_w to total energy deposited in the phantom for three different weighting factor combinations. The weighting factors in the legend refer to the weight applied to the periphery CTDI and the weight applied to the center CTDI, respectively. This plot shows that the ratio of CTDI_w to total energy deposited stays relatively flat until the beam width exceeds 10 cm. Additionally, this shows that the weighting does not have a large effect on the shape of the ratio curve, only on the magnitude.

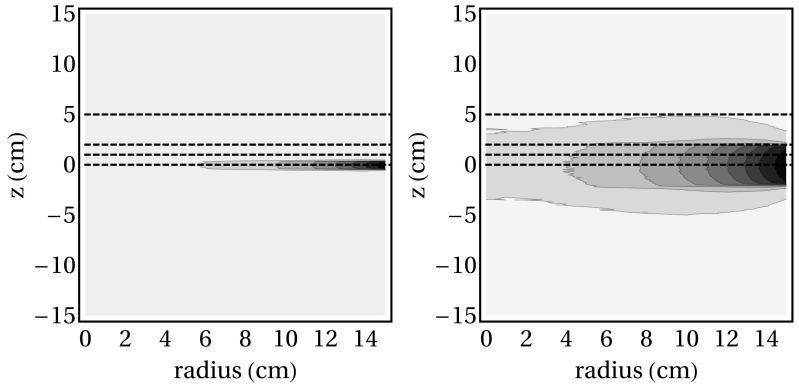

(a) 1 cm beam width

(b) 5 cm

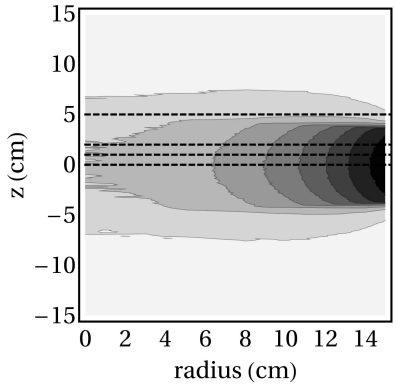

(c) 10 cm

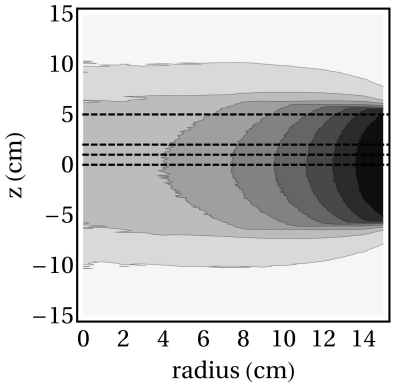

(d) 15 cm

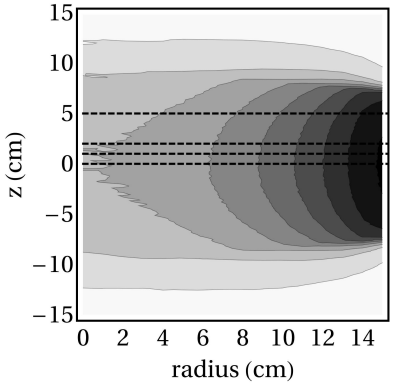

(e) 20 cm

Figure 3.14: Contours of dose along both r and z for the 32 cm diameter phantom. Dose is highest at the periphery of the cylinder and at the center of the beam path. The dashed lines represent the cuts which are shown in Figure 3.15. Each contour plot is the result of a different simulated beam width. The dose is shaded from low (white) to high (black). Actual values are shown in Figure 3.15.

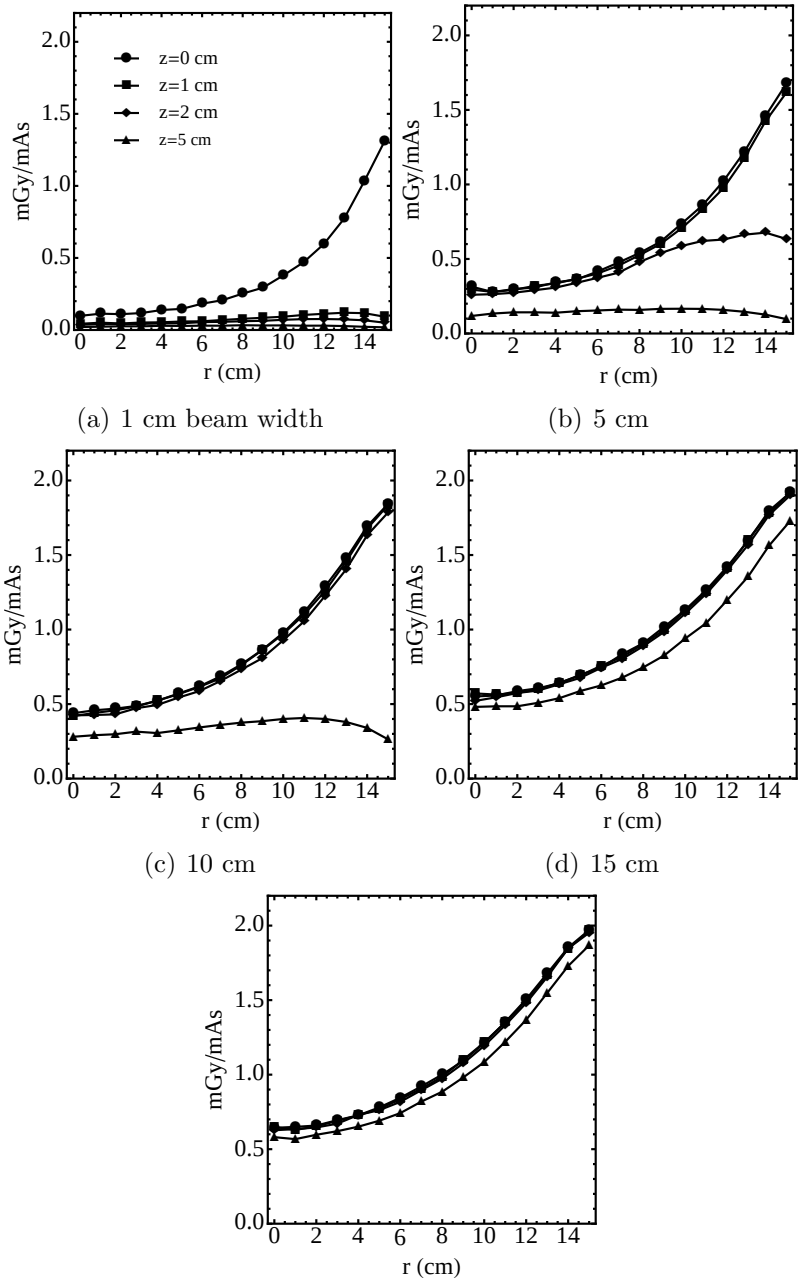

(a) 1 cm beam width

(b) 5 cm

(c) 10 cm

(d) 15 cm

(e) 20 cm

Figure 3.15: Sections of dose along r for given z for the 32 cm diameter phantom. Dose is highest at the periphery of the cylinder and at the center of the beam path. The curves are the cuts which are shown as dashed lines in Figure 3.14. Each plot is the result of a different simulated beam width.

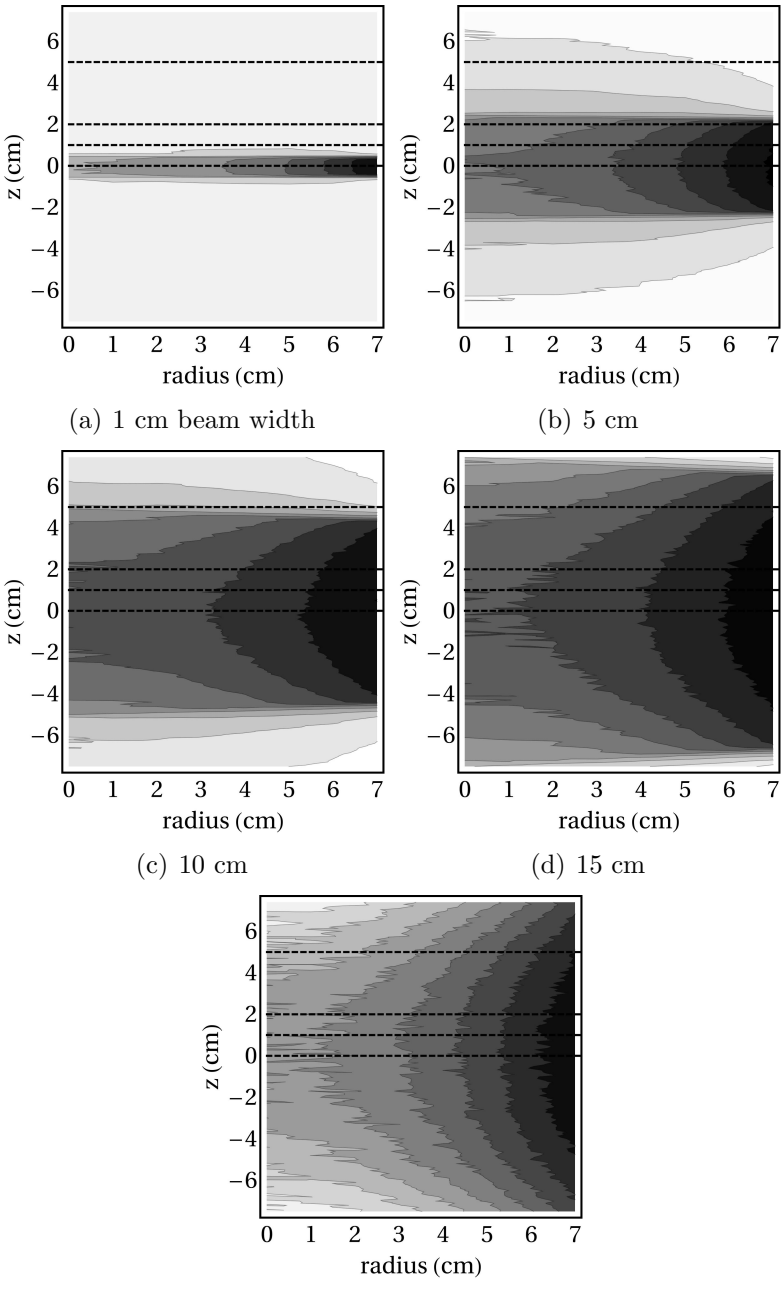

(a) 1 cm beam width

(b) 5 cm

(c) 10 cm

(d) 15 cm

(e) 20 cm

Figure 3.16: Contours of dose along both r and z for the 16 cm diameter phantom. Dose is highest at the periphery of the cylinder and at the center of the beam path. The dashed lines represent the cuts which are shown in Figure 3.17. Each contour plot is the result of a different simulated beam width. The dose is shaded from low (white) to high (black). Actual values are shown in Figure 3.17.

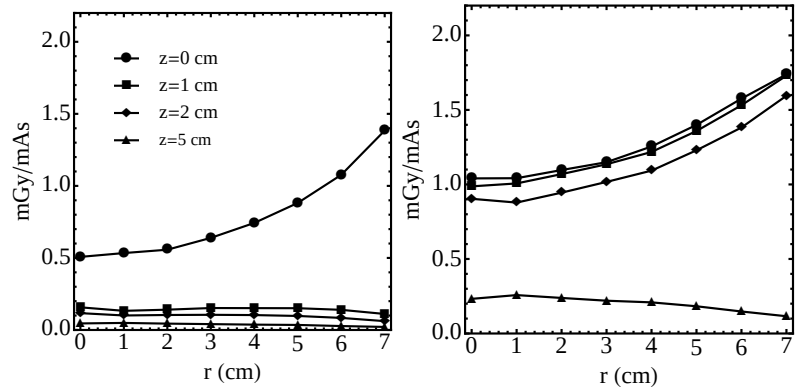

(a) 1 cm beam width

(b) 5 cm

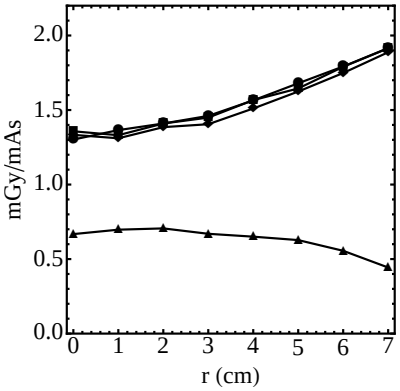

(c) 10 cm

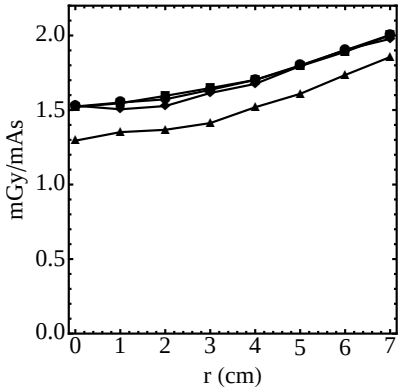

(d) 15 cm

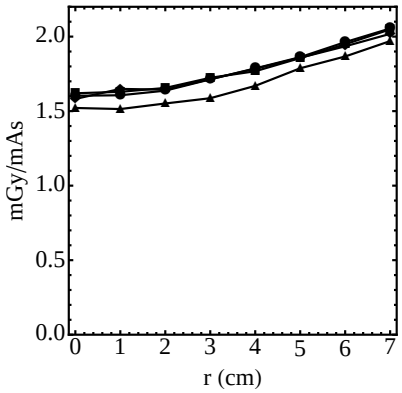

(e) 20 cm

Figure 3.17: Sections of dose along r for given z for the 16 cm diameter phantom. Dose is highest at the periphery of the cylinder and at the center of the beam path. The curves are the cuts which are shown as dashed lines in Figure 3.16. Each plot is the result of a different simulated beam width.

Chapter 4

Image Quality

4.1 Overview

4.1.1 Estimating Image Quality

A quantitative description of the object transfer properties of a CT system is necessary when evaluating image quality. Image sharpness is usually characterized and reported as a spread function, often with additional calculation of a modulation transfer function (MTF),[52, 31, 32] which is defined as the two-dimensional Fourier transform of a point spread function (PSF), the one-dimensional Fourier transform of a line spread function (LSF), or a Fourier transform of the derivative of an edge spread function (ESF).[49, 12, 53] Additionally, for a linear system, knowledge of the spread functions allow prediction of the image produced for a particular object; this prediction allows for calculations of theoretical model-based signal-to-noise ratio or detectability. Linear systems theory assumes that all objects being imaged are transferred in the same way, which is not true. CT image reconstruction is inherently a non-linear process because the image blur depends on the object to be imaged. For a computed tomography (CT) system with a poly-energetic source spectrum, objects with different energy-dependent attenuation coefficients will not be projected linearly in the imaging plane (i.e. the blur, due to scattered photons, of

the image depends on the object being imaged), even if the reconstruction algorithm or the detector transfer characteristics are linear. This is because different materials generate different amounts of scattered photons and absorb/transmit different parts of the energy spectrum in a poly-energetic beam. For a task specific evaluation of image quality it is important that the CT system blur properties are determined under the same conditions for a typical imaging task the CT system is designed for.

Many methods have been proposed for estimating the MTF of a CT system. Some have proposed a simple phantom of aluminum foil sandwiched by flat plastic slabs.[12] Others have suggested using a wire in air to estimate the PSF.[49] Still others have used bar patterns[2] or an edge.[34] Previous work exists comparing the different techniques in theory[25] and experimentally in projection imaging.[52] However, it appeared through a review of the literature that such an intercomparison of these different techniques has not yet been reported for CT systems. We investigate a comparison of MTF estimation techniques of specifically designed test objects in order to determine which is the most appropriate to evaluate the performance of a specific detection task (i.e. for a clinical modality where the patient can be represented with a fairly uniform, approximately water equivalent object, and where the detection task is mainly low contrast objects such as masses or micro calcifications).

4.2 Test-object specific line spread function and modulation transfer function of a CT imaging system

4.2.1 Methods

4.2.1.1 Test objects

Four test objects were used in this study: two thin foil objects for the slit method, and two different cube objects for the edge method.[1] The two foil test devices were constructed of a foil sandwiched between two 2.54 cm (1 inch) thick polystyrene plates. One of the foil objects was a 0.025 mm thick molybdenum, while the second was 0.1 mm thick aluminum (see Figure 4.1). One cube test object was constructed of a Polytetrafluoroethylene (Teflon) block with dimensions 2.0 cm $\times$ 2.0 cm $\times$ 5.0 cm. Figure 4.2 shows a schematic drawing, along with a picture and axial (for estimating x-y plane spread functions) and sagittal (for estimating z-axis spread functions) sections from the CT reconstruction of this object. This will be referred to as the "positive" edge object because it has a higher attenuation than the surrounding material. Teflon was chosen for its radiodensity property in the energy range of interest that was hoped would be suitable for providing a sharp edge while reducing the amount of beam-hardening artifacts. A "negative" cube test object was newly designed for this project and consisted of a cube of air that was bounded

[1]Here we use the projection radiography terms for slit and edge since the reconstruction of a foil test object results in a line pattern similar to one generated by a slit in projection radiography, while the reconstruction of a cube test object results in a square pattern similar to one generated by an edge in projection radiography.

on all six sides by polished 2.54 cm thick PMMA blocks, thus creating an edge with lower attenuation than the surrounding material. Four blocks with dimensions 2.54 cm × 2.54 cm × 5.08 cm were assembled as shown in Figure 4.3 (a). The resulting square was capped on either side by a 7.62 cm × 7.62 cm × 2.54 cm block of PMMA, resulting in a trapped cube of air, pictured in Figure 4.3 (b). Axial and sagittal sections of the reconstructed CT image of the phantom are shown in Figures 4.3 (c) and (d). The choice of low attenuation (water equivalent PMMA) material surrounding an air cube was made in order to reduce the introduction of beam-hardening artifacts into the CT reconstruction that are frequently seen with materials of high attenuation, while still allowing for an interface with a large difference in attenuation. All of the test objects were placed at the center of a water filled 14 cm diameter by 21.5 cm tall PMMA cylinder for imaging, resting on a PMMA stage. This was done so that the object specific CT system blur, as characterized by the LSFs, ESFs and MTFs, would be evaluated at the same local position. Given that CT blur not only depends on the specific test object but also on the location within the imaging field, performing the tests at effectively the same localized are will allow inter-comparison of the methods and objects. The PMMA cylinder included built-in tracking beads on the top and bottom peripheries forming circles that can be used for geometrical correction of acquired images of the test object.[40] Figure 4.4 shows the PMMA cylinder in which the test objects were placed for imaging acquisition. The two cube test objects were constructed such that the top surface was slightly slanted from the plane normal to the rotation axis, also known as the axial plane. This was done so that the slanted edge method can

be used for generating the LSF in the direction parallel to the object rotation axis, which is conventionally referred to as the z-axis (see Figure 4.5).

4.2.1.2 Image acquisition

All images were acquired using a custom-built bench-top flat-panel-based cone-beam CT scanner.[43, 44, 17] The detector used was a Varian 4030CB (Varian Corp., Salt lake City, UT) with 2046 × 1536 pixels, with 0.195 mm pixel size and a 0.6 mm columnar CsI(Tl) scintillator. The x-ray tube was a Varian B180 with an inherent filtration of 1 mm Al with 0.3 mm and 0.6 mm nominal focal spots. Additional filtration of 0.025 mm Ytterbium and a tube voltage of 100 kV was used. For all the data collection we used the 0.6 mm focal spot.

4.2.1.3 Data correction and reconstruction

The raw projection images were corrected for non-uniform gain, non-responsive pixels and the heel effect. Then, the calibrated images were geometrically corrected using a method based on estimating the inclination angles of each projected bead trajectory over the entire CT acquisition.[40] Following all image corrections, 3D volume data were reconstructed with a cubic voxel size of 0.1 mm, using a parallel implementation of the Feldkamp filtered back projection algorithm.

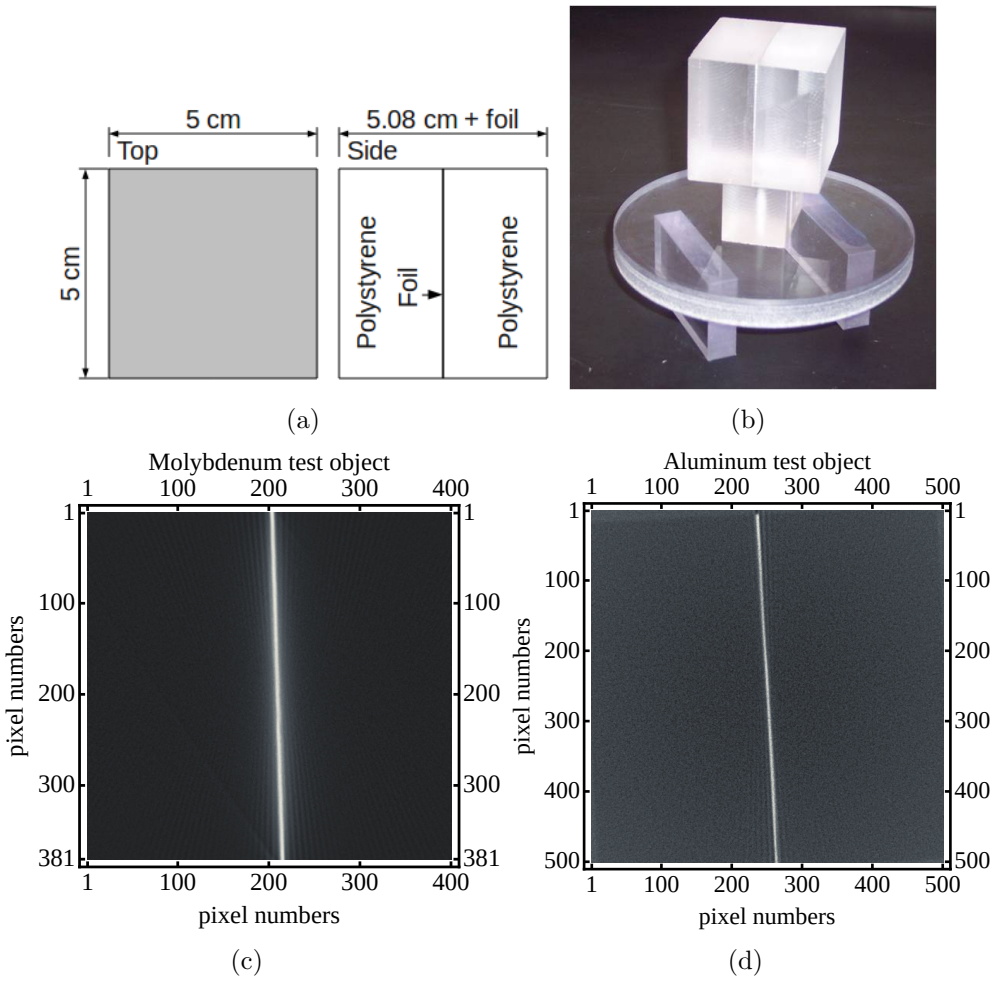

Figure 4.1: (a) Schematic representation of the foil test object. The PMMA plate dimensions are 5.0 cm × 5.0 cm × 2.54 cm. (b) Photograph of the foil test object. (c) The average of 100 axial slices of the reconstructed molybdenum foil test object. (d) The average of 100 axial slices of the reconstructed aluminum foil test object.

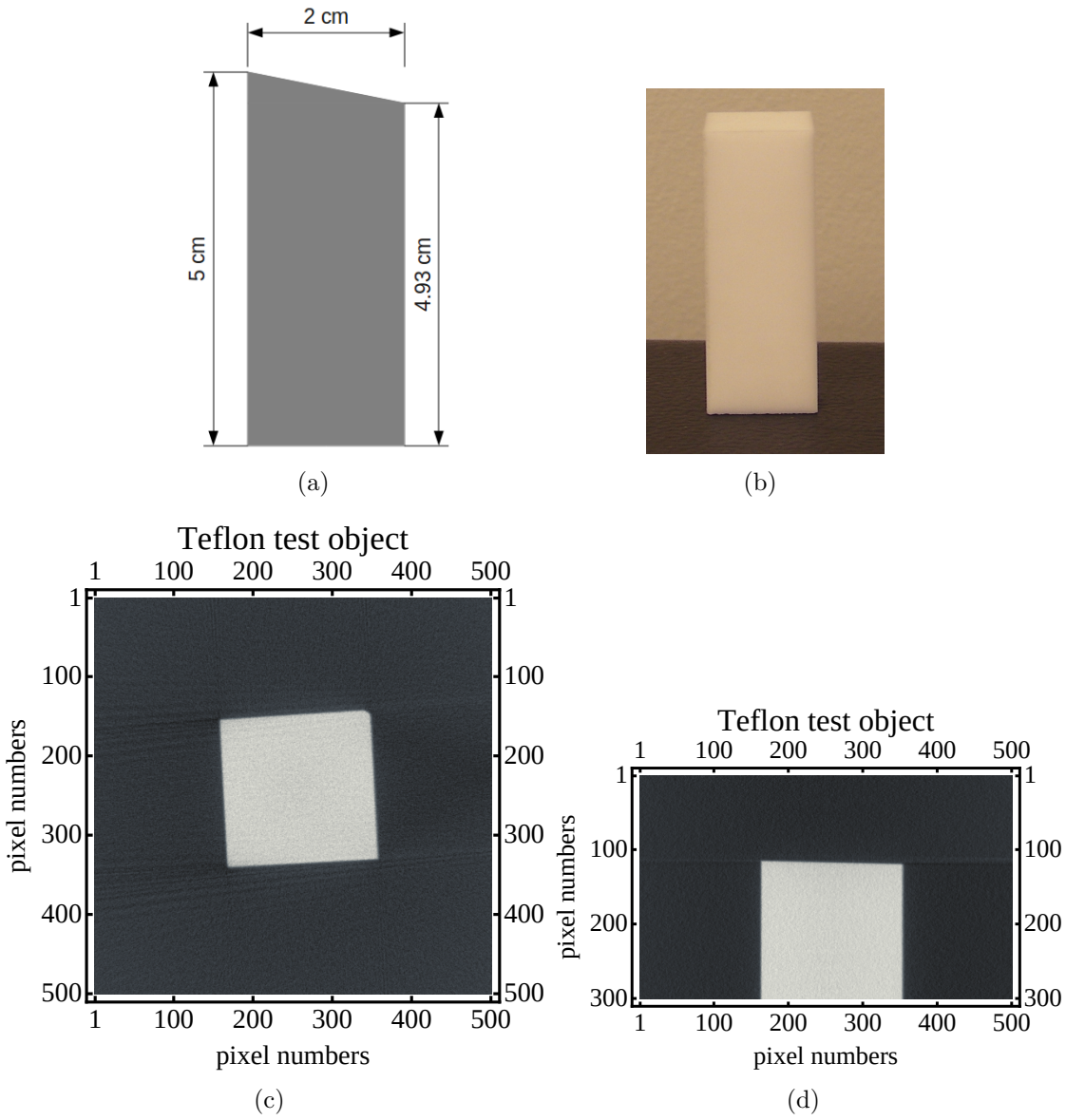

Figure 4.2: (a) Schematic drawing of the teflon cube test object. It was cut to present four edges in the x-y plane, and with a slanted edge along the top to provide a tilt along the z-axis. (b) Photograph along the longest side of the cube test object. This is a Polytetrafluoroethylene (Teflon) block with dimensions 2.0 cm $\times$ 2.0 cm $\times$ 5.0 cm. (c) The average of 100 axial slices of the reconstructed positive test object. (d) The average of 100 sagittal slices of the reconstructed positive test object.

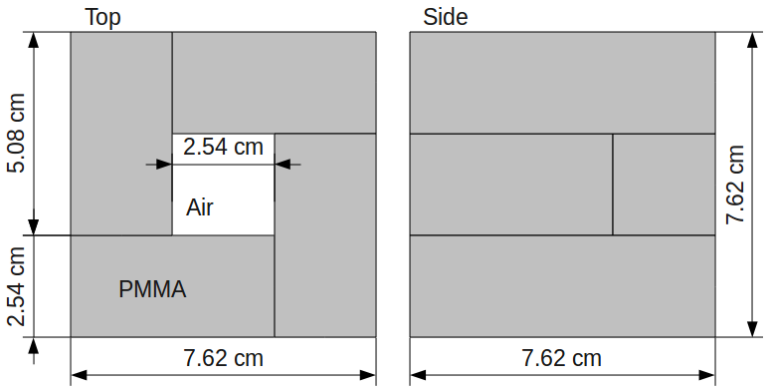

(a)

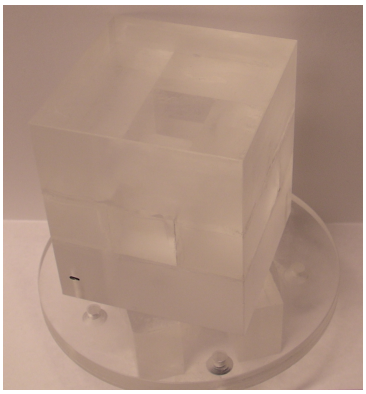

(b)

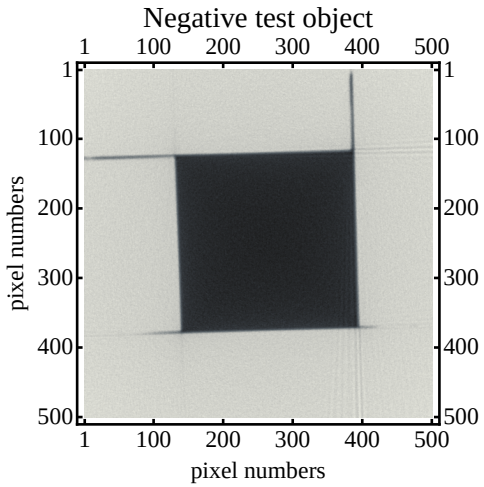

(c)

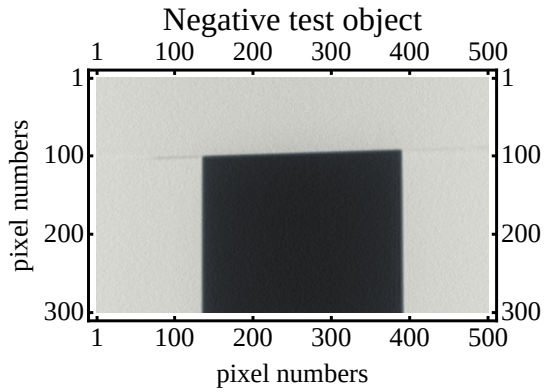

(d)

Figure 4.3: (a) Assembly of the negative cube test object. Four blocks of 2.54 cm × 2.54 cm × 5.08 cm are assembled as shown on the left to create a square of air, which is then capped on either side by a 7.62 cm × 7.62 cm × 2.54 cm block to create a trapped cube. (b) Photograph of the negative cube test object mounted on a PMMA stage. (c) The average of 100 axial slices of the reconstructed negative test object. (d) The average of 100 sagittal slices of the reconstructed negative test object

Figure 4.4: The PMMA cylinder (not filled with water), shown with the tracking beads for geometrical alignment corrections.

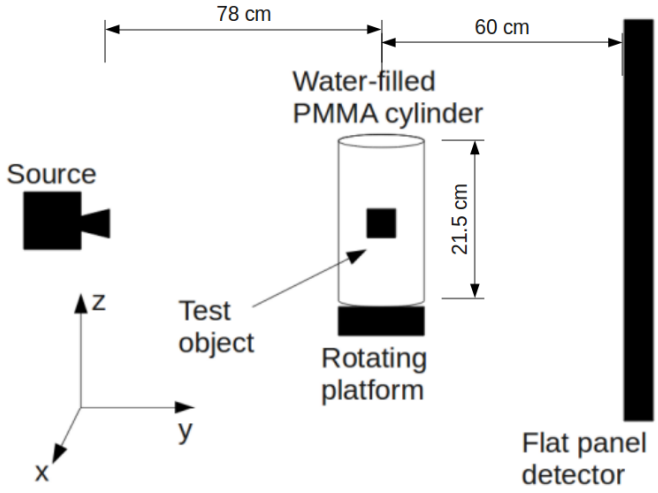

Figure 4.5: Schematic of the bench-top, cone-beam CT system.

4.2.1.4 Line and Edge spread function estimation and comparison

The estimation of the oversampled LSF or ESF was consistent with previously described computational methods. [31, 6] The volumes were reconstructed such that the edges of each test object make a small angle with the x and y axes, as shown in Figure 4.2 (c). It was not necessary to know this angle exactly prior to reconstruction, only that it be between 2 and 5 degrees. For each edge, a region of interest was selected far enough from the corners such that boundary effects could be ignored. One such region from the image of the positive phantom is shown in Figure 4.6 (a). Each row from such an ROI was taken as an estimate of the ESF of this system. However, the resolution of a single row was limited by the voxel size of the image. Because of the tilt of the object, each row was out of phase of the preceding row by a factor defined by the tilt angle. The edge of the cube test object in the region of interest was detected by taking the derivative in the direction normal to the edge, and a line was fit to the resulting maxima of the edge derivative. The slope of this line determines the offset between consecutive rows. ESFs from the out-of-phase rows are shown in Figure 4.6 (b), and the same data is shown in Figure 4.6 (c) after the offset was applied. At this point, our ESF data was no longer limited by the voxel size, but still suffers from noise, especially in the regions away from the edge. Because the angle of the edge was small, the resulting in-phase ESF data was very dense (in this case, roughly 1000 data points per voxel). It was thus reasonable to reduce the noise by averaging neighboring points (here we average every ten neighbors for both location and grayscale value), with the resulting

smoothed ESF shown in Figure 4.6 (d). A similar process was used to obtain the voxel-size-independent estimate of the LSF from the foil test objects, only in this case the derivative operation was not necessary. These ESFs and LSFs can then be used in estimating a local, object specific MTF.

For intercomparison among methods the ESF curves were converted to LSF curves. This was done by taking the derivative of the image prior to determining the high resolution spread function. The procedure described above was then used to find the voxel-size-independent, low-noise estimate of the LSFs.

4.2.1.5 Object-specific, local Modulation Transfer Function calculation

By definition, the traditional MTF assumes the system is shift-invariant and cyclic, that the CT system is linear (i.e the MTF is independent of the object measured or the system transfers all objects in the same way), and the system decomposition basis are the Fourier cosines. Such assumptions are however violated in real imaging systems, and a number of references describe the MTF limitations.[17, 18, 47, 38, 39, 37, 44, 43, 40] For this reason the MTF estimated here is designated as the local, object specific MTF (MTF_{lo}) to distinguish from the traditional MTF, as it makes the comparison of the resulting LSF/ESFs as a function of their spatial frequency mroe straight forward. The MTF_{lo} was calculated using two different previously described methods.[53, 28, 20] From the foil test object phantoms, the MTF_{lo} was calculated as the magnitude of the Fourier

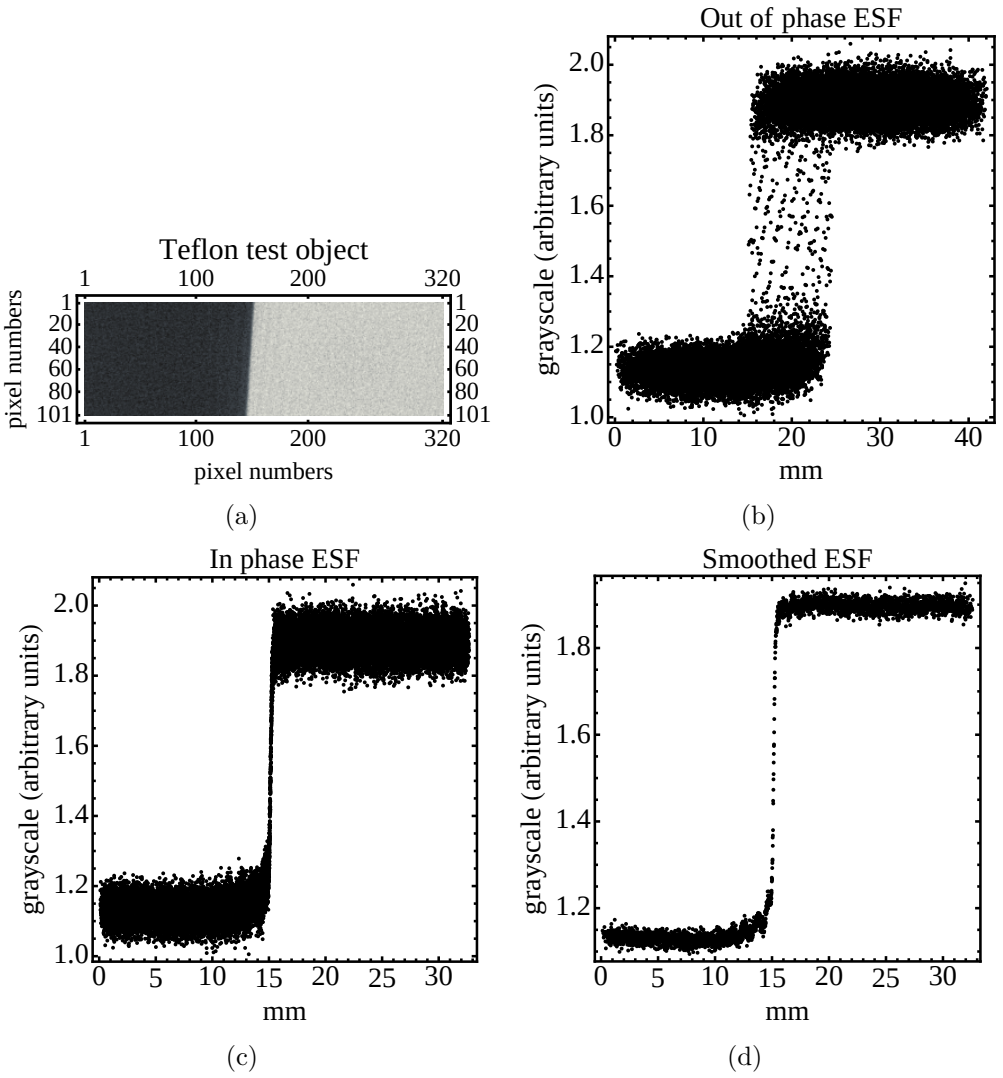

Figure 4.6: The process of going from a ROI to an estimate of a smoothed, in phase ESF is shown. (a) A sample region of interest from one edge of the positive cube test object. (b) Noisy ESF estimates that are out of phase. (c) ESF estimates that have been shifted to be in phase. (d) ESF estimates from the positive test object that have been smoothed by averaging every ten data points. Ripples from beam hardening artifacts are clearly visible at the base and apex of this edge.

transform of the estimated LSF. From the cube test object phantoms, the MTF_{lo} was calculated either directly or indirectly. To calculate the MTF_{lo} directly from the ESF integration by parts was used. To calculate the MTF_{lo} indirectly from the ESF, the derivative of the image was taken as an estimate of the LSF, and the Fourier transform of this LSF yielded an estimate of the MTF_{lo}.

4.2.2 Results

To reduce noise in the images, the average of 100 axial sections of each test object was taken. If the edges of the phantom in the x-z and y-z planes are not parallel to the long axis of the cylinder, then this averaging will increase the blur of the edges in the x-y plane. Therefore, sagittal and coronal sections of the test objects were examined, and no significant tilting of the test objects was observed (less than 100 micrometers over the length 2 cm). The foil phantoms only allow for estimation of one LSF in the x or y directions, and so we are forced to assume that the LSF in the x-y plane is rotationally symmetric using this method. The edge phantom, however, allows for estimation of four Edge or Line spread functions in the axial plane, two each along the x- and y-axes. These spread functions were found to be radially symmetric (data not shown) as the phantoms were at the center of the imaging system. Even though it was not performed here, the cube test objects would allow for estimating the off center location specific ESF/LSFs and MTF_{lo} profiles in four directions.

4.2.2.1 Axial spread functions and MTFs

The smoothed ESFs from the positive and negative test objects are shown in Figure 4.7 (a). The positive object estimates a sharper spread function, but also has ripples near the base and apex of the edge. These ESFs have been rescaled so that the base is at 0 and the peak is at 1, while the edges have been centered at 0 mm on the x-axis. The normalization was accomplished by dividing the ESFs by their respective maximum grayscale value and then subtracting their minimum value, followed by recentering such that the crest of the edge is at pixel number 0.

The central 2.0 mm of the smoothed estimates of LSF are shown in Figure 4.7 (b). The LSF curve from the foil test objects are less noisy than that obtained from the other test objects. However, the molybdenum foil exhibits a much wider spread, a curve that is significantly different than estimated by the other three test objects. Because they track one another so closely, the LSFs from the aluminum foil and negative phantom were isolated and reploted in Figure 4.7 (c). The two LSFs follow one another in the central 1 mm, but the negative object's LSF tails are lower, crossing below the x axis, demonstrating the anti-correlations of the reconstruction kernel.

The local, object specific MTFs are shown in Figure 4.8. The MTF_{lo}s shown in Figure 4.8 (a) are all calculated as the Fourier transform of the estimate of the LSF (which is the derivative of the image for the positive and negative objects). Figure 4.8 (b) shows the MTF_{lo} as estimated from the positive and negative objects only. From each object, the MTF_{lo} was estimated two ways – the direct method and

indirect method. The estimated MTFs from the same object do not match when calculated using the two methods, with the direct method MTF_{lo}s generally higher than the indirect method.

4.2.2.2 Z-axis spread functions and MTFs

The smoothed ESFs from the positive and negative test objects are shown in Figure 4.9 (a). The positive object estimates a sharper spread function as it did in the x and y directions. These ESFs have been rescaled so that the base is at 0 and the peak is at 1, while the edges have been centered at 0 mm on the x-axis. The normalization was accomplished in the same manner as for the axial slices.

Figure 4.9 (b) shows the z-axis MTF_{lo} as estimated from the positive and negative test objects only. From each object, the MTF_{lo} was estimated using the direct method. As in the axial case, the estimated MTF_{lo}s from the same object do not match when calculated using the two objects. The positive cube estimates a higher MTF_{lo} than the negative cube. It is important to note that the z-axis spread functions and MTF could not be estimated using the foil method.

4.2.3 Discussion and Conclusion

In this section we present the LSF and ESF of four test objects that can be used for MTF estimation methods. Based on previous work,[25] we expected that there will be frequency dependent differences in the results. Specifically, we expected that the edge methods perform better for estimating low-frequency response, and

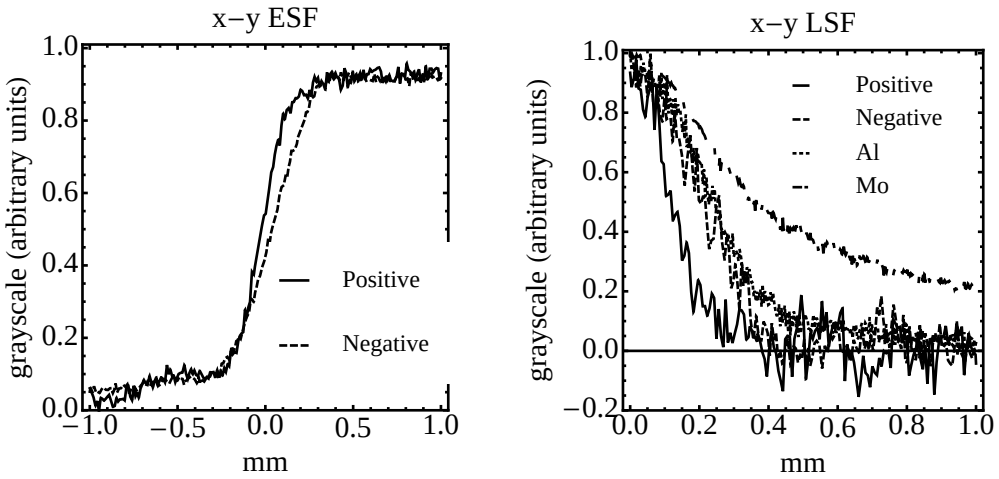

(a)

(b)

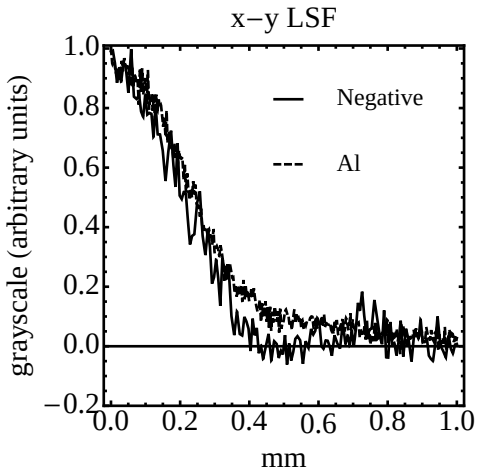

(c)

Figure 4.7: The LSF/ESF estimates using the different test objects. (a) The central 2 mm of both ESFs as obtained from the positive and negative test objects. The ESFs have been normalized and centered to allow for comparison of the relative amounts of spread. (b) 1 mm, starting at the peak, of all LSFs as obtained from the test objects. The LSFs have been normalized and centered to allow for comparison of the relative amounts of spread. The LSFs were symmetric about the peak, so only half are shown for clarity. (c) The LSFs as obtained from the aluminum foil and negative test objects. The LSFs have been normalized and centered to allow for comparison of the relative amounts of spread. The aluminum foil LSF is the dashed line, while the negative cube LSF is the solid line.

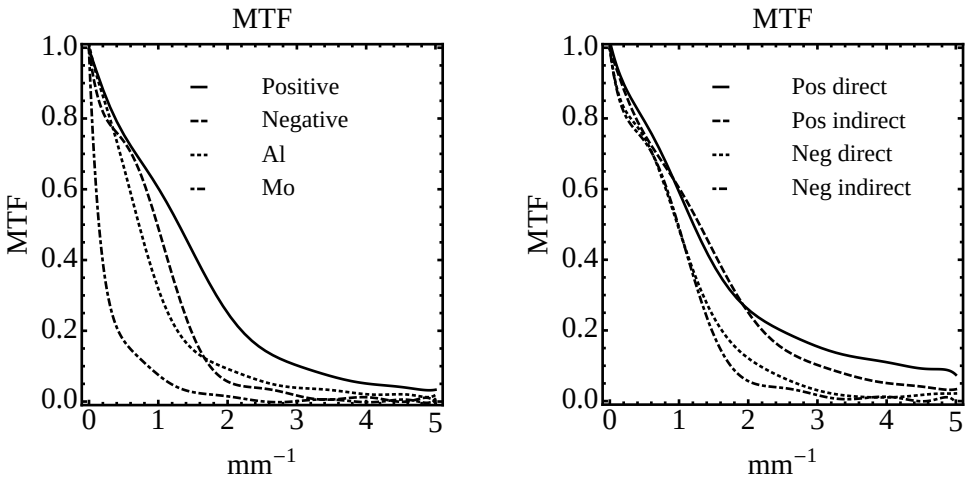

Figure 4.8: The x-y plane MTF$_{lo}$ estimates using the different test objects. (a) For the edge test objects, the derivative of the image was taken as an estimate of the LSF first, and then the Fourier transform was taken to estimate the MTF$_{lo}$. The order of curves from left to right is: Mo foil, Al foil, negative cube, positive cube. (b) The MTF$_{lo}$ as estimated by the positive and negative test objects. From each image, the MTF$_{lo}$ was calculated two ways: the direct method using integration by parts and the indirect method using the Fourier transform of the derivative of the image (an estimate of the LSF).

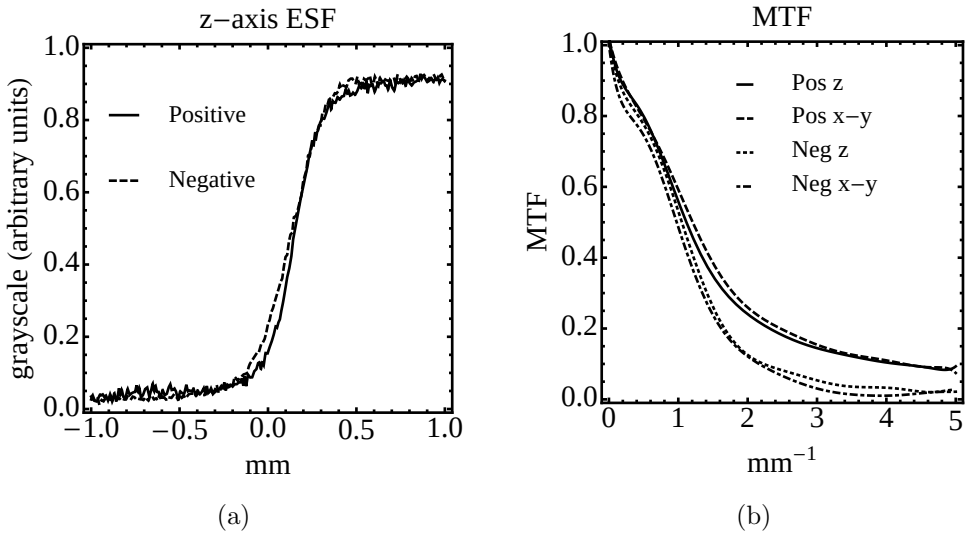

Figure 4.9: The z-axis ESF and MTF estimates using the different test objects. (a) The central 2 mm of both z-axis ESFs as obtained from the positive and negative test objects. The ESFs have been normalized and centered to allow for comparison of the relative amounts of spread. (b) The z-axis MTF as estimated by the positive and negative test objects. The MTF was calculated using the direct method described in Section 4.2.1.5. For ease of comparison, the x-y plane MTF from the cube test objects are also included.

that the slit method is superior for measuring the high-frequency response.

When examining the ESF from each test object, the negative test object shows, as expected, fewer artifacts at the base and crest of the edge than the positive test object. However, the positive test object exhibits a sharper boundary between the two materials, as shown by the presence of a steeper slope at the edge, as seen in Figure 4.7 (a). To understand where this difference arises, it is important to first identify the sources that contribute to the spread of the edge. In this system, spread comes from: 1) the fact that the source has a finite size focal spot rather than a point source (generating focal spot unsharpness), 2) the detector blur, 3) potential geometric misalignments, 4) blur generated through the back-projection algorithm, and 5) scatter generated within the phantom. The first four sources of spread are constant between the two test objects (with geometrical alignment verified by inspection in the sagittal and coronal planes), and so we must conclude that the difference arises in how much scatter from the water phantom or the test object itself reaches the detector. Because the positive phantom is more attenuating than the negative phantom, a possible explanation that some of the scattered photons generated in the surrounding water are absorbed in the higher-attenuating material. Effectively, fewer scattered photons generated in the water phantom region between the Teflon cube and the phantom walls closer to the source reach the detector, and thus it appears that the image of the positive edge contains less spread. A similar effect can be seen in the asymmetry of the ESFs. With both the positive and negative test objects, tails at the base of the ESF (corresponding to the lower attenuation material) exhibit longer, more slowly varying tails than the apex. This is also evident

from the MTF curves in Figure 4.8 (a): the low frequency drop of the negative object MTF demonstrates the presence of scatter,[42, 41, 45, 10, 11, 23] while such a low frequency drop for the positive cube is not present, thereby resulting in a much higher MTF overall. This demonstrates that measured response functions are dependent on the material being imaged, with smaller spread if higher attenuation materials are used.

In Figure 4.7 (b), it appears that foil LSFs are less noisy than the edge methods. There are two factors that contribute to the relative noise on the LSF: first, to arrive at an LSF from an ESF, a derivative must be taken. The derivative operation multiplies the transfer function in the frequency domain by a factor of $i2\pi f$, amplifying high frequency noise. This effect also explains why the MTFs as calculated by the direct and indirect methods do not match in Figure 4.8 (b). Since the high frequency noise is amplified in the derivative image, we expect deviation in the high frequency regions, as is seen here. The second reason that the foil test objects produce lower noise LSFs is that they are both metals, and, especially for the molybdenum, have high CT numbers, yielding a much larger difference between water and the peak of the LSF compared to the cube objects used in this work. The large attenuation the metal foils have is also a detriment: the molybdenum test foil method results in a larger amount of spread in the LSF. At projection angles where the x-rays must travel through the length of the foil, significant beam hardening artifacts are introduced, greatly increasing the spread in the image. The aluminum foil might still be a good option because its thickness and attenuation properties were less detrimental than the molybdenum foil, meaning it suffered less from ar-

tifact introduction. However, the few artifacts present prevent the capture of the anti-correlations seen in the tails of the negative object LSF and the low frequency bump of the MTF.

From these observations, we conclude that if one were to select a test object for estimating a spread function and MTF for a low contrast detection task in tissues that are very similar to water, either the negative test cube object or the aluminum foil object is favored. This is because one obtains from these phantoms an LSF estimate that describes the scatter characteristics of the uniform water region. Because of its higher radiodensity (Teflon is approximately 990 HU), the positive cube might be a better approximation of the spread near more opaque structures, such as bone. The molybdenum foil method, because of the large number of metal artifacts, results in a image with large spread of the LSF, and therefore we expect its applicability will be limited. The edge method allows for the estimation of the spread function and MTF along the z-axis, which is difficult to achieve using a foil based method. Even though foil based methods are used to evaluate the slice sensitivity profile of CT scanners (i.e. the point response function in the z-direction) the foil size is limited to about 2 mm diameter, therefore the over-sampled or voxel-independent LSF cannot be determined in the z-direction. With careful alignment and use of the coronal or sagittal views in addition to axial views, the cube test object provides 6 tilted edges. Thus, one can extract four ESFs in the x-y plane, and two along the z-axis, and subsequently calculate the MTF profiles in all three directions.

The results of this study are limited only to the center of the CT system

we investigated. It is important to note that the LSF and ESF of a CT imaging system are location dependent (not shift-invariant). This means that if off center measurements are taken, they are likely to differ from ESFs and LSFs measured here. However, the same methods can be used, and a profile of the imaging system's characteristics from center to periphery could be created. The cube test object allows for estimation of local asymmetric ESFs, LSFs and MTFs in three x-y and z directions. The spread functions in combination with the noise properties of CT allow estimates of low contrast detectability to be made.

Chapter 5

Summary of Conclusions

The main contribution of this thesis is the examination of the applicability of current dose and image quality metrics to modern and proposed future CT scanners. This examination shows the limitations of these metrics, and under what conditions they can be used, and under what conditions care should be taken in their application.

A secondary contribution of this thesis is a simple technique for calculating the image quality metrics in a manner that increases resolution beyond the limiting reconstructed voxel size while reducing noise. This procedure is used to derive an optimum, task-specific method for estimating image quality.

A third contribution of this thesis is a method for estimating angle-dependent spectra of clinical CT scanners, using equivalent filters. Knowledge of these angle-dependent spectra allows for statistical simulations that are faithful to actual clinical systems without relying on manufacturers' proprietary information disclosure.

Future work stemming from these projects should have two thrusts: designing a practical phantom that incorporates both dose and image quality components using the results in this thesis, and the linking of patient dosimetry estimates in Monte Carlo experiments with real world imaging studies. The ultimate goal would be real time estimation of patient organ-specific dose during CT imaging studies.

Additionaly, linking with research in radiobiology would provide a framework for converting these doses into risk factors that would be more comprehensible to the lay person undergoing a CT scan.

Bibliography

[1] Particular requirements of the safety of x-ray equipment for computed tomography. ed. 2 60601-2-44. 2001.

[2] Medical electrical equipment - characteristics of digital x-ray imaging devices - part1: Determination of the detective quantum efficiency, October 2003.

[3] *Health risks from exposure to low levels of ionizing radiation: BEIR VII phase 2*. National Academies Press, Washington, DC, 2006.

[4] *Ionizing radiation exposure of the population of the United States (Report no. 160)*. National Council on Radiation Protection and Measurements, 2009.

[5] S F Abboud, A S Badal, S H Stern, and I S Kyprianou. Designing a phantom for dose evaluation in multi-slice CT. In E Samei and N J Pelc, editors, *SPIE Medical Imaging 2010: Physics of Medical Imaging*, number 7622-762232. SPIE, 2010.

[6] S F Abboud, A S Badal, S H Stern, and I S Kyprianou. A comparison of methods for estimating the line spread function of a CT imaging system. In E Samei and N J Pelc, editors, *SPIE Medical Imaging 2011: Physics of Medical Imaging*, volume 7961. SPIE, 2011.

[7] R E Alvarez. *Extraction of Energy Dependent Information in Radiography*. PhD thesis, Stanford University, 1976.

[8] D M Bakalyar. A critical look at the numerical coefficients in CTDIvol. *Med. Phys.*, 33:2003, 2006.

[9] H.H. Barrett and W. Swindell. *Radiological Imaging: The Theory of Image Formation, Detection, and Processing*. Academic, San Diego, 1981.

[10] J M Boone. Scatter correction algorithm for digitally acquired radiographs: Theory and results. *Med. Phys.*, 13:319–328, 1986.

[11] J M Boone, B A Arnold, and J A Seibert. Characterization of the point spread function and modulation transfer functio nof scattered radiation using a digital imaging system. *Med. Phys.*, 13:254–256, 1986.

[12] John M Boone. Determination of the presampled MTF in computed tomography. *Med. Phys.*, 28:356–360, 2001.

[13] John M. Boone. The trouble with CTDI100. *Med. Phys.*, 34:1364–1371, 2007.

[14] John M. Boone. Dose spread functions in computed tomography: A monte carlo study. *Med. Phys.*, 36:4547–4554, 2009.

[15] John M Boone. Method for evaluating bow tie filter angle-dependent attenuation in CT: Theory and simulation results. *Med. Phys.*, 37:40–48, 2010.

[16] D J Brenner and E J Hall. Computed tomography - an increasing source of radiation exposure. *N Engl J Med*, 357(22):2277–2284, 2007.

[17] C C Brunner, S A Hurowitz, S F Abboud, C Hoeschen, and I S Kyprianou. Noise characterization of computed tomography using the covariance matrix. In E Samei and N J Pelc, editors, *SPIE Medical Imaging 2010: Physics of Medical Imaging*, volume 7622. SPIE, 2010.

[18] C C Brunner, B renger, C Hoeshen, and I S Kyprianou. Investigation of methods to estimate the MTF and NPS of CT towards creating an international standard. In E Samei and N J Pelc, editors, *SPIE Medical Imaging 2011: Physics of Medical Imaging*, volume 7961. SPIE, 2011.

[19] Jerrold T Bushberg, J Anthony Seibert, Edwin M Leidholdt Jr, and John M Boone. *The Essential Physics of Medcial Imaging*. Lippincott Williams and Wilkins, 2002.

[20] A Carton, D Vandebroucke, L Struye, A Maidment, Y Kao, M Albert, H Bosmans, and G Marchal. Validation of MTF measurement for digital mammography quality control,. *Medical Physics*, 32:1684–1695, 2005.

[21] Edward E Christensen, Thomas S Curry, and James E Dowdy. *An introduction to the Physics of Diagnositic Radiology*. Lea and Febiger, 1978.

[22] R. Y. L. Chu, J. Fisher, B. R. Archer, B. J. Conway, M. M. Goodsitt, S. Glaze, J. Gray, and K. J. Strauss. Standardized Methods for Measuring Diagnositc X-Ray Exposures. Technical report, AAPM, 2005.

[23] V Cooper, J M Boone, J Seibert, and C Pellot-Barakat. An edge spread technique for measurement of the scatter-to-primary ratio in mammography. *Med. Phys.*, 27:845–853, 2000.

[24] K Cranley, B J Gilmore, G W A Fogarty, and L Desponds. *IPEM Report 78, Catalogue of Diagnostic X-ray spectra and other data*. The Institue of Physics and Engineering in Medicine, 1997.

[25] I A Cunningham and B K Reid. Signal and noise in modulation transfer function determinations using the slit, wire, and edge techniques. *Med. Phys.*, 19:1037–1044, 1992.

[26] Robert L. Dixon and Adam C. Ballard. Experimental validation of a versatile system of CT dosimetry using a conventional ion chamber: Beyond CTDI100. *Med. Phys.*, 34:3399–3413, 2007.

[27] Robert L Dixon, Michael T Munley, and Ersin Bayram. An improved analytical model for CT dose simulation with a new look at the theory of CT dose. *Med. Phys.*, 32:3715–3728, 2005.

[28] Molly Donovan, Da Zhang, and Hong Liu. Step by step analysis toward optimal MTF algorithm using an edge test device. *Journal of X-Ray Science and Technology*, 17:1–15, 2009.

[29] Andrew J Einstein, Javier Sanz, Santo Dellegrottaglie, Margheritta Milite, Marc Sirol, Melena Henzlova, and Sanjay Rajagopalan. Radiation dose and cancer risk estimates in 16-slice computed tomography coronary angiography. *Journal of Nuclear Cardiology*, 15:232–240, 2008.

[30] Reza Fazel, Harlan M Krumholz, Yongfei Wang, Jersey Chen, Henry H Ting, Nilay D Shah, Khurram Nasir, Andrew J Einstein, and Brahmajee K Nallamothu. Exposure to low-dose ionizing radiation from medical imaging procedures. *N Engl J Med*, 361:849–857, 2009.

[31] Hiroshi Fujita, Du-Yih Tsai, Takumi Itoh, Kunio Doi, Junji Morishita, Katsuhiko Ueda, and Akuyoshi Ohtsuka. A simple method for determining the modulation transfer function in digital radiography. *IEEE*, 11:34–38, 1992.

[32] Maryellen Lissak Giger and Kunio Doi. Investigation of basic imaging properties in digital radiography. 1. Modulation transfer function. *Med. Phys.*, 11:287–295, 1984.

[33] J. Hsieh. *Computed Tomography: Principles, Design, Artifacts, and Recent Advances*. SPIE Press, Washington, 2003.

[34] P. F. Judy. The line spread function and modulation transfer function of a computed tomorgraphic scanner. *Medical Physics*, 3:233–236, 1976.

[35] Avinash Kak and Malcolm Slaney. *Principles of Computed Tomographic Imaging*. Institue of Electical and Electronics Engineers, 1988.

[36] Kenneth R Kase and Wlater R Nelson. *Concepts of Radiation Dosimetry*. Pergamon Press, 1978.

[37] I S Kyprianou, A Badano, B D Gallas, and K J Myers. A method to estimate the point response function of digital x-ray detectors from edge measurements. In *Medical Imaging 2007: Physics of Medical Imaging*. SPIE, 2007.

[38] I S Kyprianou, A Badano, S Park, H Liu, and K J Myers. Noise and signal detection in digital x-ray detectors using the spatial definition of SNR. In Jiang Hsieh and Ehsan Samei, editors, *SPIE Medical Imaging 2009: Physics of Medical Imaging*, volume 7258. SPIE, 2009.

[39] I S Kyprianou, G Brackman, K J Myers, A Badal, and A Badano. An efficient depth- and energy-dependent Monte Carlo model for columnar CsI detectors. In Jiang Hsieh and Ehsan Samei, editors, *SPIE Medical Imaging: Physics of Medical Imaging*, volume 69130. SPIE, 2008.

[40] I S Kyprianou, S Paquerault, B D Gallas, A Badano, S Park, and K J Myers. Framework for determination of geometric parameters of a cone beam CT scanner for measuring the system response function and improved object reconstruction. In *Biomedical Imaging: Macro to Nano. 3rd IEEE International Symposium*, pages 1248–1251, Washinton DC, 2006. ISBI, IEEE.

[41] I S Kyprianou, S Rudin, D R Bednarek, and K R Hoffmann. Study of the generalized MTF and DQE for a new microangiographic system. In *Medical Imaging 2004*, volume 5368. SPIE, 2004.

[42] I S Kyprianou, S Rudin, D R Bednarek, and K R Hoffmann. Generalizing the MTF and DQE to include x-ray scatter and focal spot unsharpness: Application to a new micro-angiogrpahic system for clinical use. *Med. Phys.*, 32(2):613–626, 2005.

[43] Iacovos S. Kyprianou, Aldo Badanao, Brandon D. Gallas, and Kyle J. Myers. Singular value description of a digital radiographic detector: Theory and measurements. *Medical Physics*, 35:4744–4756, 2008.

[44] Iacovos S. Kyprianou, Aldo Badanao, Brandon D. Gallas, Subok Park, and Kyle J Myers. A practical method for measuring the H matrix of digital x-ray and cone beam CT imaging systems. In *Society of Photo-Optical Instrumentation Engineers (SPIE) Conference Series*, volume 6142, pages 652–663, 2006.

[45] Iacovos S. Kyprianou, Arundhuti Ganguly, Stephen Rudin, Daniel R Bednarek, Brandon D Gallas, and Kyle J Myers. Efficiency of the human observer compared to an ideal observer based on a generalized NEQ which incorporates scatter and geometric unsharpness: Evaluation with a 2afc experiment. *Proc. SPIE*, pages 251–262, 2005.

[46] L. A. Lehmann, R. E Alverex, A. Macovski, W. R. Brody, N. J. Pelc, S. J. Riederer, and A. L. Hall. Generalized image combinations in dual kvp digital radiography. *Medical Physics*, 8:659–667, 1981.

[47] H Liu, I S Kyprianou, A Badano, K J Myers, R J Jennings, S Park, R V Kaczmarek, and K Chakrabarti. SKE/BKE Task based ideal observer SNR methodology for Mammography. In Jiang Hsieh and Ehsan Samei, editors, *SPIE Medical Imaging 2009: Physics of Medical Imaging*, volume 7258. SPIE, 2009.

[48] S Mori, M Endo, K Nishizawa, T Tsunoo a T Aoyama, H Fujiwara, and K Murase. Enlarged longitudinal dose profiles in cone-beam CT and the need for modified dosimetry. *Med. Phys.*, 32(4):1061–1069, 2005.

[49] Edward L Nickoloff. Measurement of the PSF for a CT scanner: appropriate wire diameter and pixel size. *Phys. Med. Biol.*, 33:149–155, 1988.

[50] J Radon. Uber die bestimmung von funktionen durch ihre integralwerte langs gewisser mannigfaltigkeiten. *Berichte uber die Verhandlungen der Sachsische Akademie der Wissenschaften*, 69:262–277, 1917.

[51] F. Salvat, J. M. Fernandez-Varea, and J. Sempau. *PENELOPE-2006: A Code System for Monte Carlo Simulation of Electron and Photon Transport*. OECD Nucelaer Energy Agency, Issy-les-Moulineaux, France, 2006.

[52] Ehsan Samei, Nicole T Ranger, James T Dobbins, and Ying Chen. Intercomparison of methods for image quality characterization. I. Modulation transfer function. *Med. Phys.*, 33:1454–1465, 2006.

[53] Nicholas J Schneiders and Stewart C Bushong. Single-step calculation of the MTF from the ERF. *Med. Phys.*, 5:31–33, 1978.

[54] J. Sempau, E. Acosta, J. Baro, J. M. Fernandez-Varea, and F. Salvat. An algorithm for monte carlo simulation of coupled electron-photon transport. *Nucl. Instrum. Meth. B*, 132:377–390, 1997.

[55] J. Sempau, J. M. Fernandez-Varea, E. Acosta, and F. Salvat. Experimental benchmarks of the monte carlo code PENELOPE. *Nucl. Instr. and Meth. B*, 207:107–123, 2003.

[56] Thoms B Shope, Robert M Gagne, and Gordon C Johnson. A method for describing the doses delivered by transmission x-ray computed tomography. *Medical Physics*, 8:488–495, 1981.

[57] D M Tucker, G T Barnes, and D P Chakraborty. Semiempirical model for generating tungsten target x-ray spectra. *Medical Physics*, 18 (2):211–218, 1991.

[58] Adam C Turner and Maria Zankl. The feasibility of a scanner-independent technique to estimate organ dose from MDCT scans: Using CTDIvol to account for differences between scanners. *Medical Physics*, 37:1816–1825, 2010.

[59] Adam C Turner, Di Zhang, Hyun J Kim, John J DeMarco, Chris H Cagnon, Erin Angel, Dianna D Cody, Donna M Stevens, Andrew N Primak, Cynthia H McCollough, and Michael F McNitt-Gray. A method to generate equivalent energy spectra and filtration models based on measurement for multidetector CT monte carlo dosimetry simulations. *Medical Physics*, 36:2154–2164, 2009.

[60] Habib Zaidi and Xie George Xu. Computational anthropomorphic models of the human anatomy: the path to realistic Monte Carlo modeling in radiolgical sciences. *Annual Review of Biomedical Engineering*, 9:471–500, 2007.